



Multiplicative topological semimetalsAdipta Pal ^{1,2}, Joe H. Winter,^{1,2,3} and Ashley M. Cook ^{1,2,*}¹Max Planck Institute for Chemical Physics of Solids, Nöthnitzer Strasse 40, 01187 Dresden, Germany²Max Planck Institute for the Physics of Complex Systems, Nöthnitzer Strasse 38, 01187 Dresden, Germany³SUPA, School of Physics and Astronomy, University of St. Andrews, North Haugh, St. Andrews KY16 9SS, United Kingdom

(Received 9 February 2023; accepted 30 November 2023; published 22 January 2024)

Exhaustive study of topological semimetal (TSM) phases of matter in equilibrated electronic systems and myriad extensions has built upon the foundations laid by earlier introduction and study of Weyl semimetals, with broad applications in topologically protected quantum computing, spintronics, and optical devices. We extend recent introduction of multiplicative topological phases to find previously overlooked TSM phases of electronic systems in equilibrium, with minimal symmetry protection. We show these multiplicative TSM (MTSM) phases exhibit rich and distinctive bulk-boundary correspondence and response signatures that greatly expand understanding of consequences of topology in condensed matter settings, such as the limits on Fermi arc connectivity and structure, and transport signatures such as the chiral anomaly. In this paper, we therefore lay the foundation for extensive future study of MTSMs.

DOI: [10.1103/PhysRevB.109.035147](https://doi.org/10.1103/PhysRevB.109.035147)**I. INTRODUCTION**

Topological semimetals (TSMs) are a vast family [1,2] of topological phases of matter studied in great depth experimentally [3–12] in the search for tabletop, quasiparticle realizations of high-energy physics [13]. At the simplest level, the topological degeneracies of band structures in these TSM phases are realized quite generically if either time-reversal symmetry [14] or inversion symmetry [15] is broken. This is the requirement for twofold topological degeneracies characteristic of the Weyl semimetal (WSM) phase, although it is desirable to realize such degeneracies in the vicinity of the Fermi level [16,17], with minimal contributions to the Fermi surface from other electronic states. In such cases, the key signatures of WSMs are especially prominent, including the distinguishing Fermi arc surface states [18–23] and transport signatures associated with the chiral anomaly [24–30]. Such isolation of Weyl nodes in the vicinity of the Fermi level is also facilitated—and the physics of TSMs enriched—by systematic study of these topological phases in compounds with wide-ranging phenomena, including superconductivity, strong spin-orbit coupling, and strong correlations [31–37]. Much progress has also been made in identifying other TSMs with more complex topological degeneracies [2,38–41] in electronic band structures, protected by a large

set of crystalline point group symmetries in combination with additional antiunitary symmetries such as time reversal.

In this paper, we return to the foundations of TSM studies by introducing previously unidentified TSM phases of matter of electronic systems in equilibrium, which may then be generalized in the same manner as outlined above. We do so by studying the first TSM realizations of multiplicative topological phases, a recently identified set of topological phases of matter described by Bloch Hamiltonians in an infinitely large, periodic bulk, which are symmetry-protected tensor products of parent Bloch Hamiltonians. Here, we note that multiplicative topological phases are distinct from square root topological phases [42–48], which are based on matrix multiplication rather than tensor products.

We therefore introduce multiplicative TSM (MTSM) phases as all TSMs with symmetry-protected multiplicative (tensor product) structure by first introducing the multiplicative WSMs (MWSMs), characterized by Hamiltonians for multiplicative topological phases constructed specifically from tensor products of WSM Bloch Hamiltonians.

We first review the WSM phase and its canonical models. We then construct examples of MTSM phases using these past results. The MTSMs are then characterized in the bulk and their bulk-boundary correspondence established.

II. REVIEW OF THE WSM PHASE AND SUITABLE MODELS FOR CONSTRUCTING MULTIPLICATIVE PHASES

The WSM is a topologically nontrivial phase of matter characterized by topologically protected, doubly-degenerate and linearly dispersing band crossings in the Brillouin zone (BZ) [13]. That is, these band crossings, known as Weyl points or nodes, cannot be removed from the electronic structure through smooth deformations of the Hamiltonian but rather

*cooka@pks.mpg.de

only through mutual annihilation of the Weyl nodes by bringing two nodes of opposite topological charge to the same point in the BZ to gap out these band touchings. When the Fermi level intersects only the Weyl nodes of this semimetal phase, their low-energy physics dominates, yielding a variety of intensely studied exotic phenomena of interest for applications. At the simplest level, the Weyl nodes serve as quasiparticle, tabletop realizations of Weyl fermions predicted in high-energy physics [49]. However, they are also a starting point in going well beyond high-energy physics by tilting the Weyl cone to realize a type-II WSM phase [1], in which the low-energy physics of the Weyl nodes is not Lorentz invariant.

WSM phases can be realized in effectively noninteracting systems where certain discrete symmetries are broken rather than respected, in contrast to many other effectively noninteracting topological phases. They may be derived through symmetry breaking starting from the Dirac semimetal (DSM) state [39,40], for instance (which could be topologically robust or finetuned), by breaking either time-reversal symmetry \mathcal{T} or inversion symmetry \mathcal{I} , which pulls the two Weyl nodes comprising the Dirac node away from one another in momentum space [50]. This phase, characterized by Weyl nodes in the BZ, is topologically stable if Weyl nodes of opposite topological charge do not annihilate one another [51].

\mathcal{I} -breaking WSM phases are of tremendous experimental interest but are described by Bloch Hamiltonian models with four bands at minimum. A more natural starting point in deriving MTSM phases is instead to use the minimal WSM Bloch Hamiltonian achieved by breaking \mathcal{T} , which possesses only two bands. Such two-band models for the WSM correspond to the nontrivial homotopy group $\pi_3(S^2)$ and similarly to the two-band Chern insulators (CIs) and Hopf insulators [52] and the two-band Kitaev chain model [53], which may be combined using known constructions [54] to form a multiplicative counterpart of the WSM phase, the MWSM phase.

We therefore consider a well-established two-band Bloch Hamiltonian previously used to study Weyl nodes, with various instances of this model serving as the parents of the MWSM:

$$\mathcal{H}_{\text{WSM}}(\mathbf{k}) = t_1 \sin k_x \tau^x + t_2 \sin k_y \tau^y + t_3(2 + \gamma - \cos k_x - \cos k_y - \cos k_z) \tau^z. \quad (1)$$

where τ^j ($j = x, y, z$) are the Pauli matrices in the orbital basis. The two band spectrum:

$$E(\mathbf{k}) = \pm \sqrt{t_1^2 \sin^2 k_x + t_2^2 \sin^2 k_y + \epsilon(\mathbf{k})^2}, \quad \epsilon(\mathbf{k}) = t_3(2 + \gamma - \cos k_x - \cos k_y - \cos k_z), \quad (2)$$

has two gapless nodes at $\mathbf{k} = (0, 0, \pm k_0)$, for $\cos k_0 = \gamma$. We refer to these as the Weyl nodes. The equation of motion for Bloch electrons in the \mathbf{k} space in the presence of Berry curvature is represented by $\dot{\mathbf{r}} = \mathbf{v}_{\mathbf{k}} + \dot{\mathbf{k}} \times \mathbf{F}(\mathbf{k})$. Here, $\mathbf{F}(\mathbf{k})$ is the Berry curvature, $\mathbf{v}_{\mathbf{k}}$ is the group velocity of the electron, and \mathbf{r} is the position space coordinate. For the equation of motion to remain invariant under \mathcal{T} symmetry, one must have the equality $\mathbf{F}(\mathbf{k}) = -\mathbf{F}(-\mathbf{k})$. The breaking of \mathcal{T} symmetry then involves a minimum of two Weyl nodes with opposite Berry curvature at opposite momenta. Therefore, close to the

Weyl nodes, we have

$$\mathcal{H}_{\pm}(\mathbf{k}) = \pm t_1 k_x \tau^x + t_2 k_y \tau^y \pm t_3 \sin k_0 k_z \tau^z, \quad (3)$$

which in turn corresponds to the Berry curvatures:

$$\mathbf{F}^{\pm}(\mathbf{k})|_{0,0,\pm k_0} = \pm \frac{t_1 t_2 t_3 \sin k_0}{2[t_1 k_x^2 + t_2 k_y^2 + (t_3 \sin k_0)^2 k_z^2]^{3/2}} \mathbf{k}. \quad (4)$$

The Chern number of the lower-energy band for the range $k_x = 0$, $k_y = 0$, and $k_z \in (-k_0, k_0)$ is $C = \pm 1$ depending on the direction of the magnetic field corresponding to the monopoles at the two Weyl points. The Weyl nodes are involved with exotic boundary states at surfaces perpendicular to the z axis, called the Fermi arc surface states. For the case where the surfaces are open in the x direction, the surface dispersion is given by

$$E(k_y) = \pm t_2 \sin k_y, \quad (5)$$

and the arc states

$$\Psi(x, k_y, k_z) = \exp(+ik_y y + ik_z z) \times [\exp(-\lambda_1 x) - \exp(-\lambda_2 x)] \frac{1}{\sqrt{2}} \begin{pmatrix} 1 \\ \pm i \end{pmatrix}.$$

In the \mathbf{k} space, this includes all contours $\cos k_y + \cos k_z > 1 + \cos k_0$.

III. MWSM IN THE BULK

A protocol for constructing the child Hamiltonian for the MWSM, \mathcal{H}_c derived from \mathcal{H}_{p1} and \mathcal{H}_{p2} as reported by Cook and Moore [54], is given as follows. Given two two-band Bloch Hamiltonians \mathcal{H}_{p1} and \mathcal{H}_{p2} written in a general form, with momentum dependence suppressed, as

$$\mathcal{H}_{p1} = \begin{pmatrix} a & b \\ c & d \end{pmatrix}, \quad \mathcal{H}_{p2} = \begin{pmatrix} \alpha & \beta \\ \gamma & \delta \end{pmatrix}, \quad (6)$$

the multiplicative child Bloch Hamiltonian constructed from these two parents can be written as \mathcal{H}_{12}^c , where

$$\mathcal{H}_{12}^c = \begin{pmatrix} a\delta & -a\gamma & b\delta & -b\gamma \\ -a\beta & a\alpha & -b\beta & b\alpha \\ c\delta & -c\gamma & d\delta & -d\gamma \\ -c\beta & c\alpha & -d\beta & d\alpha \end{pmatrix}. \quad (7)$$

Expressing the two-band parent Bloch Hamiltonians $\mathcal{H}_{p1}(\mathbf{k})$ and $\mathcal{H}_{p2}(\mathbf{k})$ more compactly as the following:

$$\mathcal{H}_{p1}(\mathbf{k}) = \mathbf{d}_1(\mathbf{k}) \cdot \boldsymbol{\tau}, \quad \mathcal{H}_{p2}(\mathbf{k}) = \mathbf{d}_2(\mathbf{k}) \cdot \boldsymbol{\sigma}, \quad (8)$$

where $\mathbf{d}_1(\mathbf{k})$ and $\mathbf{d}_2(\mathbf{k})$ are momentum dependent, three-component vectors of scalar functions, and each of $\boldsymbol{\sigma}$ and $\boldsymbol{\tau}$ is the vector of Pauli matrices, the multiplicative child Hamiltonian may more compactly be written as

$$\mathcal{H}_{12}^c(\mathbf{k}) = (d_{11}, d_{21}, d_{31}) \cdot \boldsymbol{\tau} \otimes (-d_{12}, d_{22}, -d_{32}) \cdot \boldsymbol{\sigma} \quad (9)$$

to highlight the tensor product structure of the child Hamiltonian, which can be symmetry protected, as discussed by Cook and Moore [54] on multiplicative topological phases, and therefore can describe phases of matter, even in the presence of additional bands.

The tensor-product structure guarantees that the energy spectrum of the child Hamiltonian is a product of the energy

spectrum of $\mathcal{H}_{p1}(\mathbf{k})$, i.e., $E_{p1}(\mathbf{k})$, and of $\mathcal{H}_{p2}(\mathbf{k})$, i.e., $E_{p2}(\mathbf{k})$, respectively:

$$E_{12}^c(\mathbf{k}) = \pm E_{p1}(\mathbf{k})E_{p2}(\mathbf{k}). \quad (10)$$

This implies that bands of the child Hamiltonian dispersion are at least doubly degenerate everywhere in the bulk BZ.

We will consider two cases in this paper: (1) The Weyl node separation of each parent is along one axis in the BZ, and (2) the axis along which Weyl nodes are separated in one parent is perpendicular to the axis along which Weyl nodes are separated in the other parent. Spectral and magnetotransport properties differ significantly between these two cases, as we will show, demonstrating the richness of MTSM phases of matter.

A. MWSM—Parallel axis parents

The construction of the MWSM for both parents along the same axis is derived from two parent WSMs. As an example, we consider the following parents and the resulting child:

$$\begin{aligned} \mathcal{H}_{p1}(\mathbf{k}) &= t_{11} \sin k_x \tau^x + t_{21} \sin k_y \tau^y \\ &+ t_{31}(2 + \gamma_1 - \cos k_x - \cos k_y - \cos k_z) \tau^z, \end{aligned} \quad (11a)$$

$$\begin{aligned} \mathcal{H}_{p2}(\mathbf{k}) &= t_{12} \sin k_x \sigma^x + t_{22} \sin k_y \sigma^y \\ &+ t_{32}(2 + \gamma_2 - \cos k_x - \cos k_y - \cos k_z) \sigma^z, \end{aligned} \quad (11b)$$

$$\begin{aligned} \mathcal{H}_c(\mathbf{k}) &= [t_{11} \sin k_x \tau^x + t_{21} \sin k_y \tau^y \\ &+ t_{31}(2 + \gamma_1 - \cos k_x - \cos k_y - \cos k_z) \tau^z] \\ &\otimes [-t_{12} \sin k_x \sigma^x + t_{22} \sin k_y \sigma^y \\ &- t_{32}(2 + \gamma_2 - \cos k_x - \cos k_y - \cos k_z) \sigma^z]. \end{aligned} \quad (11c)$$

Each parent Hamiltonian realizes Weyl nodes at $\mathbf{k} = (0, 0, \cos^{-1} \gamma_i)$ when $-1 < \gamma_i < 1$, ($i = 1, 2$). Examples of such topologically nontrivial dispersion are shown in Figs. 1(a) and 1(b), respectively.

From these parent Hamiltonian dispersions, we can find the dispersion of the child. As given in Eq. (10), the bulk spectrum is doubly degenerate and determined by the spectra of the parent 1, $E_{p1}(\mathbf{k})$, and parent 2, $E_{p2}(\mathbf{k})$, respectively, which take the following forms:

$$\begin{aligned} E_{p1}(\mathbf{k}) &= [t_{11}^2 \sin^2 k_x + t_{21}^2 \sin^2 k_y + \epsilon_1(\mathbf{k})^2]^{1/2}, \\ E_{p2}(\mathbf{k}) &= [t_{12}^2 \sin^2 k_x + t_{22}^2 \sin^2 k_y + \epsilon_2(\mathbf{k})^2]^{1/2}, \end{aligned} \quad (12)$$

where $\epsilon_{i/2}(\mathbf{k}) = t_{3i/2}(2 + \gamma_{i/2} - \cos k_x - \cos k_y - \cos k_z)$.

For the sake of convenience, we refer to the MWSM with Weyl node separation for each parent along the same axis in the BZ [as in the case of parents given by Eqs. (11a) and (11b)] as MWSM||. For the MWSM|| bulk spectrum given by Eqs. (10) and (12), gapless points occur at the positions in the BZ where gapless points are present for the parent systems. As γ_1 and γ_2 control separation of the Weyl nodes in the BZ for the parents, they play a major role in determining the number of nodes, the location of the nodes, and the polynomial order of the nodes in the BZ for the child. When $\gamma_1 = \gamma_2$, for instance, we have two gapless points, but the dispersion near the nodes is quadratic. In contrast, for $\gamma_1 \neq \gamma_2$ as for parents depicted in Figs. 1(a) and 1(b), the child MWSM|| has four

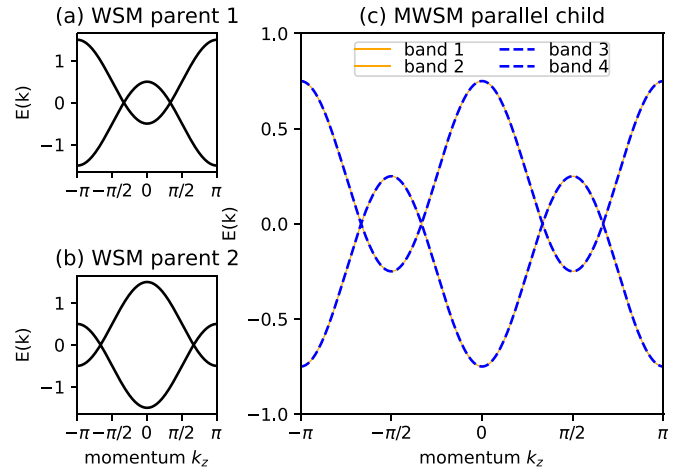


FIG. 1. Dispersion $E(\mathbf{k})$ for (a) Weyl semimetal (WSM) parent Hamiltonian with $\gamma_1 = 0.5$ along k_z and $t_{11} = t_{21} = t_{31} = 1$, (b) WSM parent Hamiltonian with $\gamma_2 = -0.5$ along k_z and $t_{12} = t_{22} = t_{32} = 1$, and (c) the resulting multiplicative WSM (MWSM) parallel child Hamiltonian along k_z . Other momenta components are set as zero.

nodes, and bands disperse linearly in the vicinity of the nodes, as shown in Fig. 1(c). Each node is fourfold degenerate.

While such degeneracy naively suggests Dirac or Weyl nodes of higher charge, the multiplicative nodes are distinct in a number of ways. To examine this difference, we look at the child Hamiltonian in the vicinity of each multiplicative node for the case $-1 < \gamma_1 \neq \gamma_2 < 1$. From the tensor product structure, it is easy to check that $\frac{\partial E_{\pm}}{\partial k_i} = \text{const.}$, which implies that the dispersion is linear at each of the gapless nodes of the MWSM. Therefore, the possibility of a higher-order Weyl node is nullified. The positions of each of the multiplicative nodes are determined by the nodes in the respective parents. We refer to $(0, 0, \pm k_{01})$ as the Weyl node positions derived from the first parent and $(0, 0, \pm k_{02})$ as that from the second parent. Here, $\gamma_i = \cos k_{0i}$, ($i = 1, 2$). If the gapless point is $(0, 0, k_{02})$, then we define MWSM|| in the vicinity as $\mathcal{H}_{||,2}^c$, and

$$\begin{aligned} \mathcal{H}_{||,2}^c &= t_{31}(\gamma_1 - \gamma_2) \\ &\times \tau^z(-t_{12}k_x\sigma^x + t_{22}k_y\sigma^y - t_{32}\sin k_{02}\bar{k}_{z,2}\sigma^z), \end{aligned} \quad (13)$$

where $\bar{k}_{z,2} = (k_z - k_{02})$. Surprisingly, this looks like a DSM Hamiltonian, whose Dirac node has been shifted in \mathbf{k} space. Since it is no longer at the origin, the time-reversal symmetry is broken. For the other node, $\gamma_1 = \cos k_{01}$ for $(0, 0, k_{01})$, we define the multiplicative Hamiltonian in the vicinity as $\mathcal{H}_{||,1}^c$, so that

$$\begin{aligned} \mathcal{H}_{||,1}^c &= (t_{11}k_x\tau^x + t_{21}k_y\tau^y + t_{31}\sin k_{01}\bar{k}_{z,1}\tau^z) \\ &\times t_{32}(\gamma_1 - \gamma_2)\sigma^z, \end{aligned} \quad (14)$$

where $\bar{k}_{z,1} = (k_z - k_{01})$, which contains off-diagonal terms for the block Hamiltonian. Again, it is possible to perform a similarity transformation on this Hamiltonian, in the form $U = R_{\tau}^{-1}(\theta, \phi) \otimes R_{\sigma}(\theta, \phi)$, so that we get another shifted

DSM-type Hamiltonian:

$$\begin{aligned} \bar{H}_{||,1}^c &= t_{32}(\gamma_1 - \gamma_2) \\ &\times \tau^z(t_{11}k_x\sigma^x + t_{21}k_y\sigma^y + t_{31}\sin k_{0,1}\bar{k}_{z,1}\sigma^z). \end{aligned} \quad (15)$$

Again, the shift from the origin breaks the time-reversal symmetry of the original DSM. It is therefore appropriate to refer to the MWSM|| as possessing degeneracies consisting of Weyl nodes rather than possessing Dirac nodes, exhibiting strikingly different physics as a result.

B. MWSM—Perpendicular axis parents

Before characterizing bulk-boundary correspondence and transport signatures of MTSMs, we explore further richness of multiplicative constructions by considering cases where parent Weyl nodes are separated along orthogonal axes in \mathbf{k} space. As a specific case, we choose parent Hamiltonians such that the first parent has Weyl node separation along the y axis, the second along the z axis:

$$\begin{aligned} \mathcal{H}_{p1}(\mathbf{k}) &= t_{11}\sin k_x\tau^x + t_{21}\sin k_z\tau^y \\ &+ t_{31}\left(2 + \gamma_1 - \sum_i \cos k_i\right)\tau^z, \end{aligned} \quad (16a)$$

$$\begin{aligned} \mathcal{H}_{p2}(\mathbf{k}) &= t_{12}\sin k_x\sigma^x + t_{22}\sin k_y\sigma^y \\ &+ t_{32}\left(2 + \gamma_2 - \sum_i \cos k_i\right)\sigma^z. \end{aligned} \quad (16b)$$

Again, the bulk spectrum is derived from the tensor product structure:

$$\begin{aligned} E_{p1}(\mathbf{k}) &= [t_{11}^2\sin^2 k_x + t_{21}^2\sin^2 k_z + \epsilon_1^2(\mathbf{k})]^{1/2}, \\ E_{p2}(\mathbf{k}) &= [t_{12}^2\sin^2 k_x + t_{22}^2\sin^2 k_y + \epsilon_2^2(\mathbf{k})]^{1/2}, \\ E_{\perp}^c(\mathbf{k}) &= \pm E_{p1}(\mathbf{k})E_{p2}(\mathbf{k}), \end{aligned} \quad (17)$$

where $\epsilon_{1/2}(\mathbf{k}) = t_{31/32}(2 + \gamma_{1/2} - \cos k_x - \cos k_y - \cos k_z)$. Examples of parent and child dispersion in this case are shown in Fig. 2 for the values $\gamma_1 = -0.5$ and $\gamma_2 = 0.5$.

We gain greater understanding of the multiplicative structure in this case by examining the low-energy expansion of the child Hamiltonian in the vicinity of its nodes. Taylor expanding up to linear order around the point $(0, k_{0,1}, 0)$ for $\gamma_1 = \cos k_{0,1}$, one gets

$$\begin{aligned} \mathcal{H}_{\perp,1}^c(\mathbf{k}) &= (t_{11}k_x\tau^x + t_{21}k_z\tau^y + t_{31}\sin k_{0,1}\bar{k}_{y,1}\tau^z) \\ &\otimes [t_{22}\sin k_{0,1}\sigma^y - t_{32}(\gamma_2 - \gamma_1)\sigma^z]. \end{aligned} \quad (18)$$

Similarly, expanding around $(0, 0, k_{0,2})$ for $\gamma_2 = \cos k_{0,2}$, we get

$$\begin{aligned} \mathcal{H}_{\perp,2}^c(\mathbf{k}) &= [t_{21}\sin k_{0,2}\tau^y + t_{31}(\gamma_1 - \gamma_2)\tau^z] \\ &\otimes (-t_{12}k_x\sigma^x + t_{22}k_y\sigma^y - t_{32}\sin k_{0,2}\bar{k}_{z,2}\sigma^z). \end{aligned} \quad (19)$$

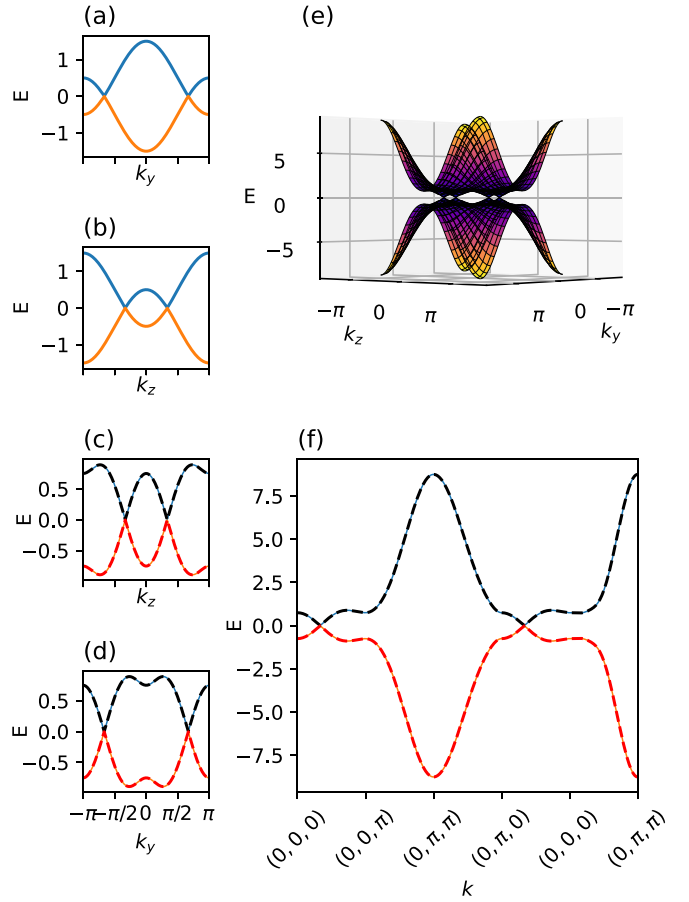


FIG. 2. Dispersion $E(k)$ ($t_{11} = t_{12} = 1$, $t_{21} = t_{22} = 1$, and $t_{31} = t_{32} = 1$) for (a) Weyl semimetal (WSM) parent Hamiltonian with $\gamma_1 = -0.5$ along k_y ($k_x = k_z = 0$), (b) WSM parent Hamiltonian with $\gamma_2 = 0.5$ along k_z ($k_x = k_y = 0$), and the resulting multiplicative WSM (MWSM) perpendicular child Hamiltonians along (c) k_z ($k_x = k_y = 0$) and (d) k_y ($k_x = k_z = 0$). The energy dispersions plotted along both k_y and k_z are shown in (e), and the dispersion along a high-symmetry path in the first quadrant of the two-dimensional (2D) Brillouin zone (BZ) is shown in (f). Inversion symmetry relates the nodes in the first quadrant to those in the other quadrants, giving rise to four gapless nodes in the 2D BZ.

One notices that $\mathcal{H}_{\perp,2}^c(\mathbf{k})$ is equivalent to a DSM [8,40] when $\gamma_1 = \gamma_2$.

C. MWSM—Parent axes at relative angle θ

We briefly consider a more general MWSM construction in which the Weyl axis of one parent is rotated relative to the Weyl axis of the second parent by a general angle θ , which we denote MWSM θ . (The MWSM|| and MWSM \perp cases then correspond to $\theta = 0$ and $\theta = \frac{\pi}{2}$, respectively.) Below, we provide the Hamiltonian for such a system. The Hamiltonians for parents 1 and 2 as well as the multiplicative child Hamiltonian are, respectively,

$$\begin{aligned} \mathcal{H}_{p1}(\mathbf{k}) &= t_{11}\sin k_x\tau^x + t_{21}\sin k'_y\tau^y + t_{31}(2 + \gamma_1 \\ &- \cos k_x - \cos k'_y - \cos k'_z)\tau^z, \end{aligned} \quad (20a)$$

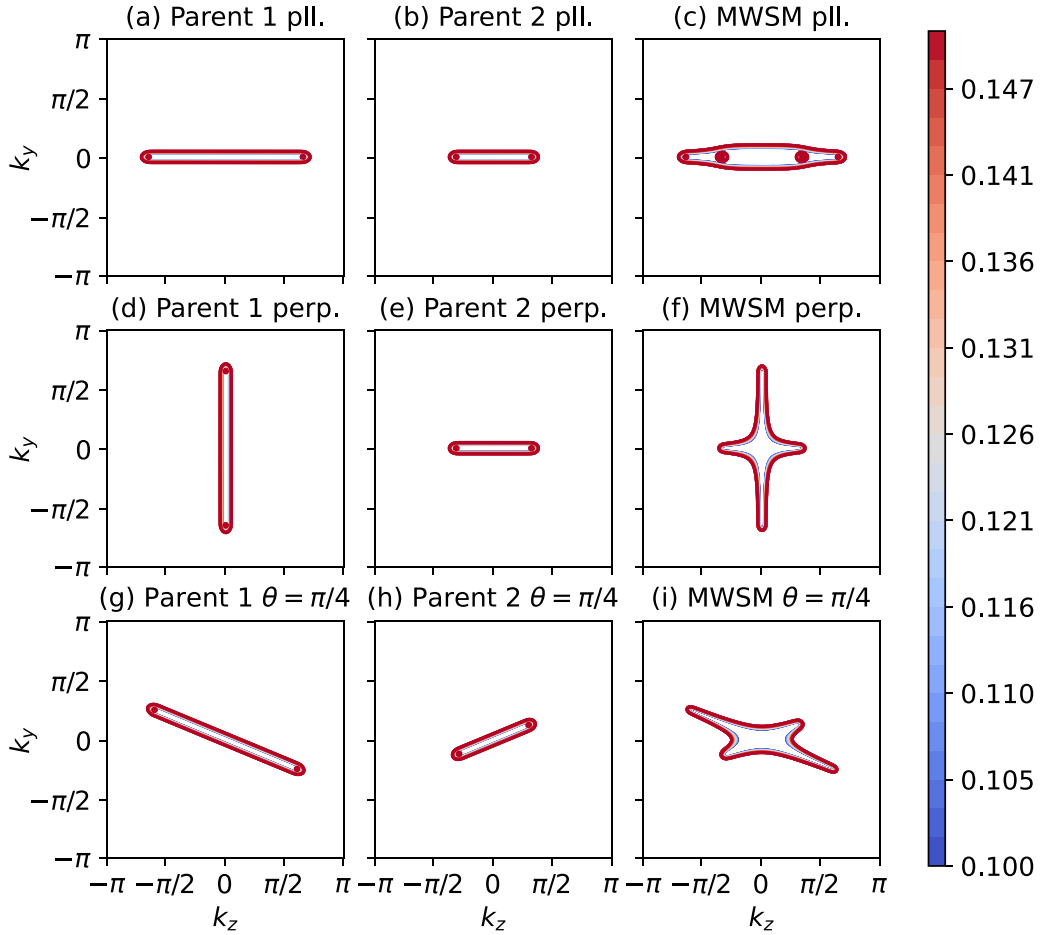


FIG. 3. Fermi arcs for different configurations of the parent systems. In the first row, we show Fermi arcs for (a) and (b) parents both having Weyl axes along z and (c) child for the multiplicative Weyl semimetal (MWSM) parallel system. The second row shows Fermi arcs for (f) the MWSM perpendicular system with (d) parent 1 having Weyl axis along y and (e) parent 2 with Weyl axis along z . The final row displays the case when the Weyl axes (g) and (h) parent systems are at a relative angle $\theta = \frac{\pi}{4}$ with (i) the child system. We have set the Weyl node separation as $\gamma_1 = -0.5$ for parent 1 and $\gamma_2 = 0.5$ for parent 2 in all cases. All the Fermi arcs correspond to energy contours within the interval $[0.1t, 0.15t]$, where $t = t_{ij} = 1$.

$$\mathcal{H}_{p2}(\mathbf{k}) = t_{12} \sin k_x \sigma^x + t_{22} \sin k_y'' \sigma^y + t_{32} (2 + \gamma_2 - \cos k_x - \cos k_y'' - \cos k_z'') \sigma^z, \quad (20b)$$

$$\begin{aligned} \mathcal{H}_c(\mathbf{k}) = & [t_{11} \sin k_x \tau^x + t_{21} \sin k_y' \tau^y + t_{31} (2 + \gamma_1 - \cos k_x - \cos k_y' - \cos k_z') \tau^z] \\ & \otimes [-t_{12} \sin k_x \sigma^x + t_{22} \sin k_y'' \sigma^y - t_{32} (2 + \gamma_2 - \cos k_x - \cos k_y'' - \cos k_z'') \sigma^z]. \end{aligned} \quad (20c)$$

Here, $\mathbf{k}' = R_x(\frac{\theta}{2})\mathbf{k}$ and $\mathbf{k}'' = R_x(-\frac{\theta}{2})\mathbf{k}$, where $R_x(\phi)$ denotes a rotation about the k_x axis by angle ϕ . Examples of Fermi arc configurations for the parents and corresponding MWSM in this case are shown in Figs. 3(g)–3(i), respectively, for $\theta = \pi/4$. Like the MWSM \perp Fermi arcs shown in Fig. 3(f), the child Fermi arcs exhibit a crosslike structure, but it is skewed for the more general θ case. While this suggests the general θ case might be well understood from the perpendicular case, we expect this case could be quite interesting: Notably, the MWSM \parallel and \perp derived from parents defined over square lattices in real space are also defined over a square lattice, with additional neighbor hoppings. For

general θ , however, the child Hamiltonian may instead be defined on an effective moiré lattice even if each parent is individually defined on a square lattice, like systems considered by Dunbrack and Cano [55].

D. Discrete symmetries of the MWSM

The discrete symmetries satisfied by the parent WSMs include invariance under particle-hole conjugation given by $\mathcal{P} = \sigma^x \kappa$, such that the Hamiltonian satisfies

$$\sigma^x \mathcal{H}_{1/2}^*(\mathbf{k}) \sigma^x = -\mathcal{H}_{1/2}(-\mathbf{k}),$$

and invariance under spatial inversion given by $\mathcal{I} = \sigma^z$, such that the Hamiltonian satisfies

$$\sigma^z \mathcal{H}_{1/2}(\mathbf{k}) \sigma^z = \mathcal{H}_{1/2}(-\mathbf{k}).$$

The MWSM \parallel or \perp child systems are instead invariant under time reversal given by $\mathcal{T} = i\tau^x \sigma^x \kappa$, corresponding to the transformation:

$$\tau^x \sigma^x \mathcal{H}_c^*(\mathbf{k}) \tau^x \sigma^x = \mathcal{H}_c(-\mathbf{k}).$$

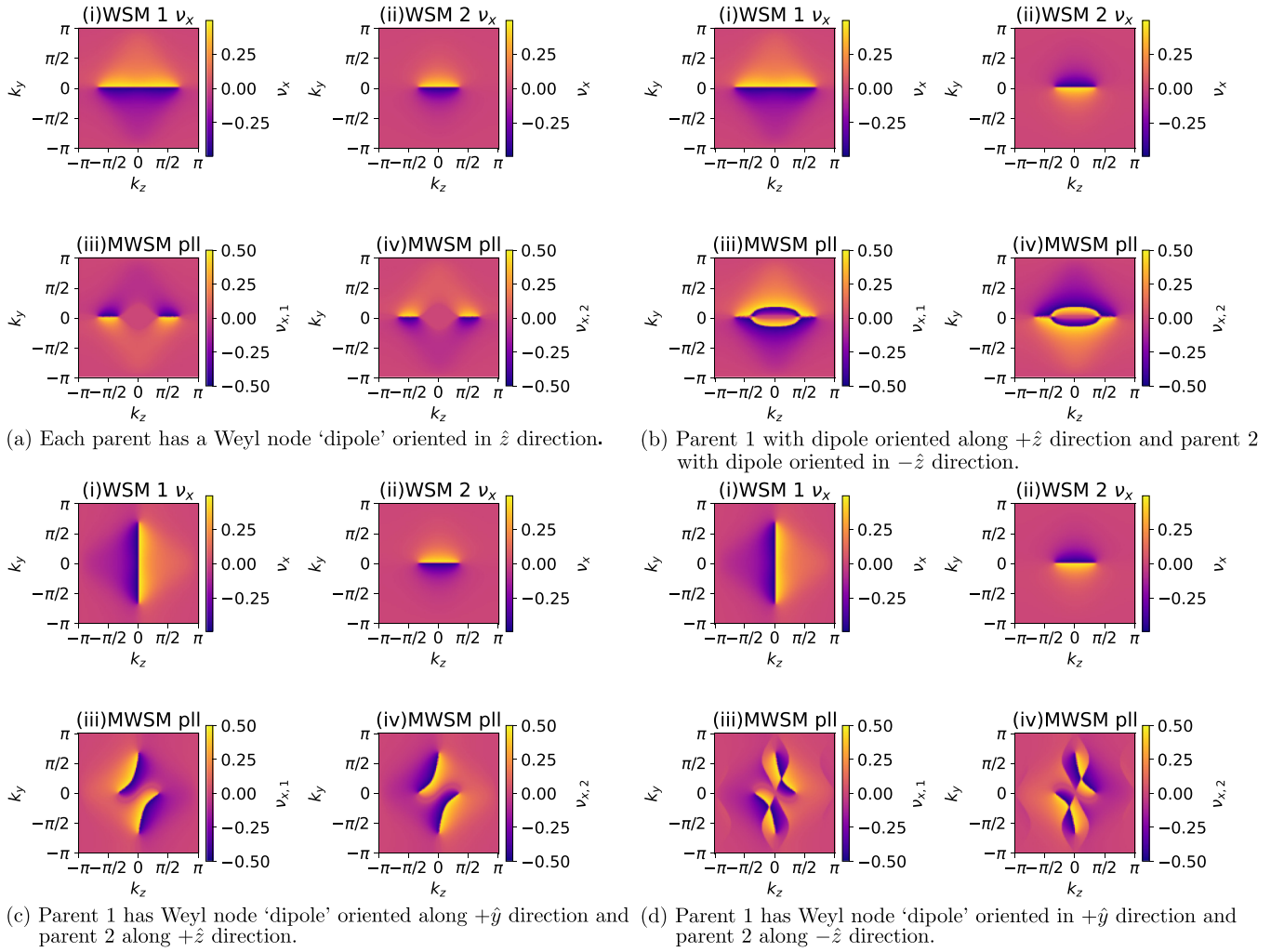


FIG. 4. Wannier spectra in multiplicative Weyl semimetal (MWSM) parallel and MWSM perpendicular for two filled bands derived from Wilson loop around k_x for parent 1 with $\gamma_1 = -0.5$ and parent 2 with $\gamma_2 = 0.5$. (a) and (b) have opposite orientation of the Weyl node dipole for parent 2, as do (c) and (d). Both the corresponding Wannier eigenvalues of the MWSM for the two degenerate lowest-energy occupied bands are shown separately in the second rows of (a)–(d).

They are also invariant under spatial inversion given by $\mathcal{I} = \tau^z \sigma^z$, corresponding to the transformation:

$$\tau^z \sigma^z \mathcal{H}_c(\mathbf{k}) \tau^z \sigma^z = \mathcal{H}_c(-\mathbf{k}).$$

The MWSM should then satisfy the symmetry $\mathcal{T}' = \mathcal{T}\mathcal{I}$, which may also protect the DSM phase. Indeed, in some cases, the Dirac Hamiltonian for the MWSM near the nodes is reminiscent of the corresponding low-energy Hamiltonian for a DSM. This invariance of the multiplicative bulk Hamiltonian under products of transformations, which leave each parent Hamiltonian invariant, is expected given the multiplicative dependence of the child on the parents.

E. Bulk characterization of topology with Wilson loops

As calculated in Supplemental Material Sec. S1 [56], the Berry connection for the MWSM is given as

$$\mathbf{A} = (A_{1,k_x} - A_{2,k_x}, A_{1,k_y} - A_{2,k_y}, A_{1,k_z} - A_{2,k_z}), \quad (21)$$

where $A_{j,l} = (i\langle +_j | \partial_l | +_j \rangle, i\langle -_j | \partial_l | -_j \rangle)$. Using this expression for the Berry connection, we compute Wilson loops and associated Wannier spectra by integrating over k_x for a given k_y and k_z , as detailed by Alexandradinata *et al.* [57]. Here, we decompose the Wannier spectrum of the degenerate occupied subspace of the child Hamiltonian into two parts, corresponding to the two Wannier orbitals, to highlight the complementary structures in the Wannier spectra and the fact that they are also distinguished by whether the relevant state in the degenerate manifold is a tensor product of an occupied state from parent 1 and unoccupied state from parent 2 or vice versa. In the parallel case illustrated in Fig. 4(a), the Wannier spectra derived from Wilson loop calculations show that only in regions where only one of the parent phases is nontrivial do we get nontrivial Wannier spectra distinguished by π values for Wannier charge centers. However, the Wannier spectra in the region where each parent is topological appears trivial, given the dependence of child Wannier spectra on parent Wannier spectra distinctive of multiplicative topological phases. We have referred to a pair of Weyl nodes of equal and

opposite topological charge as a *dipole*. We observe that the orientation of this dipole due to the two constituent parents is important, as antiparallel dipoles, as depicted in Fig. 4(b), show nontrivial Wilson loop eigenvalues in a region in the two-dimensional (2D) BZ, where neither of the parent systems have nontrivial topological character. Analogous results for the MWSM \perp are shown in Fig. 4(d), although the Wannier spectrum structure is far richer than in the parallel case. The mod 1 constraint in the Wannier spectra fails to characterize the case where the parents are both topological. To resolve this situation, we discuss an alternate strategy below.

F. Bulk characterization of topology with Euler numbers

The approach using Wilson loops fails to characterize the topology in regions where both the parents are topological. In the case of the MWSM parallel system, there exists an alternate approach derived from the discrete symmetries of the child system. The $(\mathcal{T}')^2 = +1$ symmetry implies that there is an alternate basis where $\mathcal{T}' = \kappa$. Therefore, it is possible to convert the child Hamiltonian into a purely real system, as done in similar systems in a previous study [58]. We provide the details in Supplemental Material Sec. S4 [56]. We use the fact that the MWSM parallel case can be understood in terms of stacking of multiplicative CIs (MCIs) in parallel along the k_z direction as discussed later in Sec. IV C and consider the topology derived from each such MCI parallel system. This allows us to express the topology of the MCI at a given k_z in terms of two Euler numbers given by

$$E_I = q_1 + q_2, \quad E_{II} = q_1 - q_2, \quad (22)$$

where q_1 and q_2 are, respectively, the skyrmion numbers of the parent two-band systems. A MWSM \parallel with each parent topologically nontrivial is then characterized by the pair $(E_I, E_{II}) = (2, 0)$. If parent 1 is topological but parent 2 is instead trivial, however, $(E_I, E_{II}) = (1, 1)$. In Sec. IV C, we demonstrate that this bulk characterization successfully determines bulk-boundary correspondence in the case of the MWSM \parallel .

IV. MWSM WITH OPEN-BOUNDARY CONDITIONS

A. Slab spectra of MWSM

An important aspect of WSM physics is its distinctive bulk-boundary correspondence: Weyl nodes in the three-dimensional (3D) bulk BZ serve as termination points of topologically protected boundary states known as Fermi arcs when projected to a slab BZ corresponding to open boundary conditions in one direction. We expect analogous topologically protected surface states in MTSMs and explore possible realizations of these Fermi arc states in this section.

One might expect that the tensor product structure of the multiplicative phases is visible in the surface spectrum of the MWSM. Numerical simulations show that this is the case. For the parent WSMs, the surface spectra is given as $E(k_y) \sim \sin(k_y)$ [Figs. 5(a), 4(b), and 6, second row] (analytically calculated in Supplemental Material Sec. S2 [56]) for nodes along the z axis and open boundaries along the x direction and $E(k_z) \sim \sin(k_z)$ (Fig. 6, first row) for nodes along the y axis and open boundaries along the x direction. Indeed,

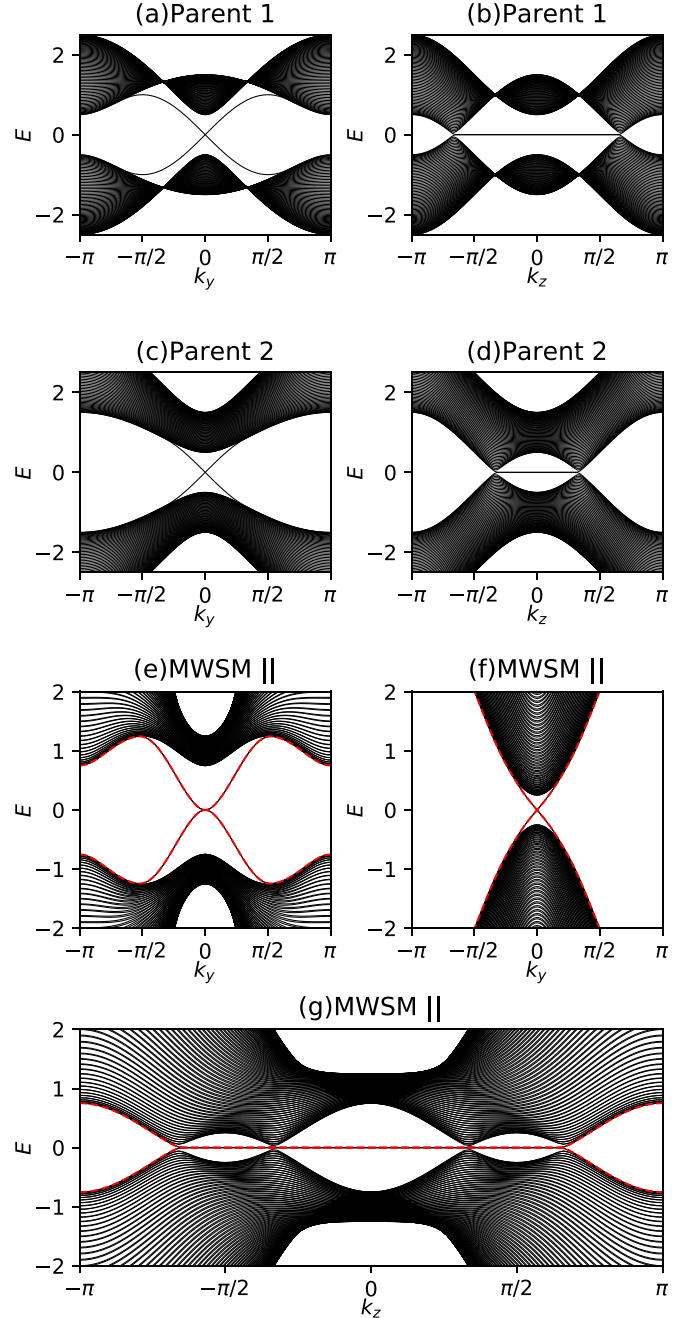


FIG. 5. Finite slab spectra (in the x direction, $L_x = 80$) along k_y ($k_z = 0$) and k_z ($k_y = 0$), respectively, for (a) and (b) Weyl semimetal (WSM) with $\gamma_1 = -0.5$, (c) and (d) WSM with $\gamma_2 = 0.5$. (e) and (f) Slab spectra ($L_x = 80$) E vs k_y for the multiplicative WSM (MWSM) \parallel child created from the above two parents for $k_z = 0$ and $k_z = \frac{\pi}{2}$, respectively. (g) Slab spectra E vs k_z at $k_y = 0$ for the same MWSM \parallel child system. Twofold degeneracies in the child slab spectra are highlighted by dashed red and black lines.

corresponding surface spectra of child Hamiltonians depend on these surface spectra in a multiplicative way. Numerical simulation from Fig. 5(e) shows that, for MWSM \parallel , the slab spectra disperses as $E(k_y) \sim \sin^2(k_y)$ for two parents each with surface spectrum $E(k_y) \sim \sin(k_y)$. In contrast, the lower-

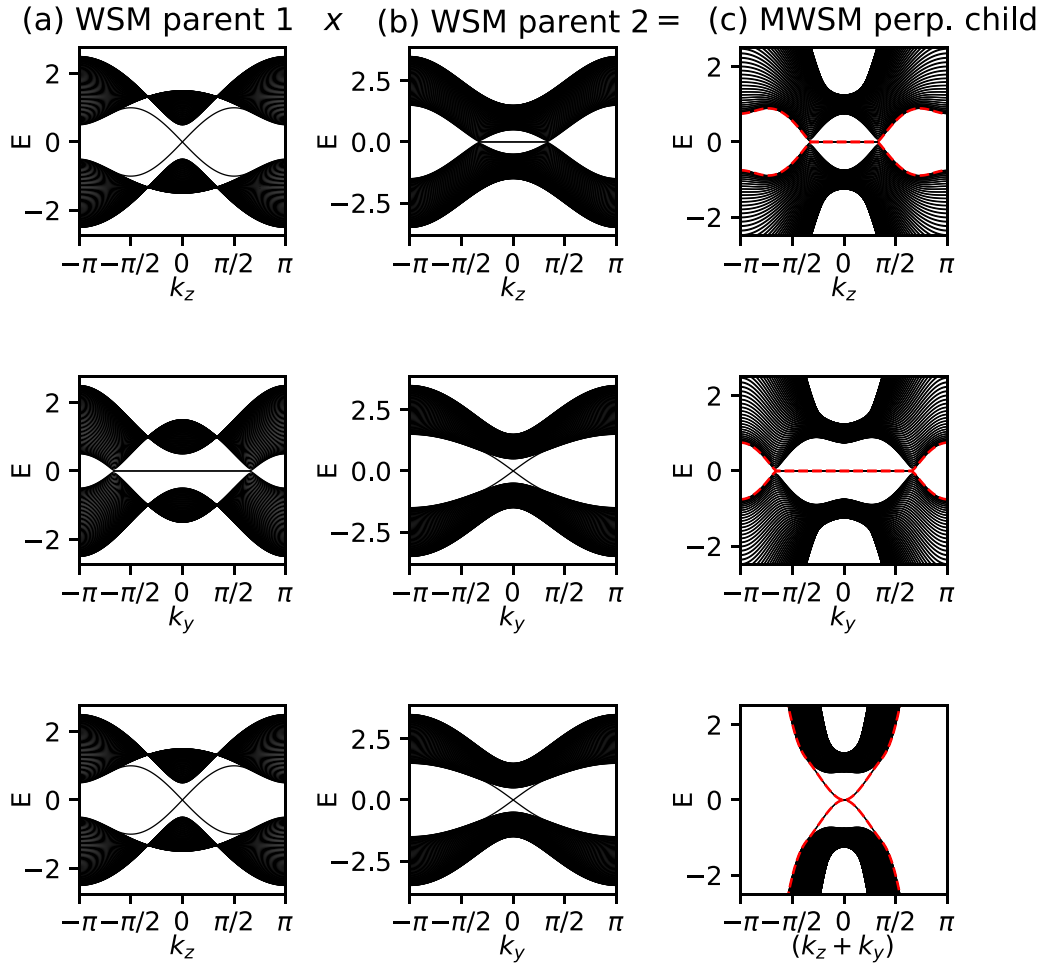


FIG. 6. Finite slab spectra (in the x direction, $N_x = 80$) with the constituent parent Hamiltonians: (a) Weyl semimetal (WSM) parent Hamiltonian 1 with $\gamma_1 = -0.5$ and Weyl nodes along the k_y direction, (b) WSM parent Hamiltonian 2 with $\gamma_2 = 0.5$ with Weyl nodes along the k_z direction, and (c) the multiplicative WSM (MWSM) perpendicular child Hamiltonian. It is apparent how the surface spectra along k_z (for $k_y = 0$) and k_y (for $k_z = 0$) combine multiplicatively to create the surface spectra for the MWSM perpendicular system. The lowest diagram along column (c) especially shows the spectra along the diagonal $k_z + k_y$ direction where the component spectra $\sin(k_z)$ and $\sin(k_y)$ have combined to produce $\sin(k_z) \sin(k_y)$ as the leading term. Twofold degeneracies in the child slab spectra are highlighted by dashed red and black lines.

most plot in Fig. 6(c) shows that the surface spectrum instead disperses as $E(k_y, k_z) \sim \sin(k_y) \sin(k_z)$ for MWSM \perp when one parent has the former surface spectrum and the other has the latter. We also show that the case of each parent surface spectrum along k_z , which exhibits flat bands between the two Weyl nodes [Figs. 5(b) and 5(d)], corresponds to flat bands between all four gapless points in the MWSM parallel system [Fig. 5(g)]. However, fitting $\sin^2(k_y)$ curves to each of the parallel and perpendicular MWSM spectra reveals that, except in special cases when $\gamma_1 = \gamma_2$ where the fit is exact, the slab spectra does not disperse as $\sin^2(k_y)$ and instead exhibits k_z dependence. One can check this by comparing E vs k_y slab spectra in the range $-\min(k_{0,1}, k_{0,2}) < k_z < \min(k_{0,1}, k_{0,2})$ and $\min(k_{0,1}, k_{0,2}) < k_z < \max(k_{0,1}, k_{0,2})$. The spectra appear linear near zero in the latter case. We show the Fermi arcs for the MWSM systems where the Weyl axes of the parents are parallel, perpendicular, and at a relative angle $\theta = \frac{\pi}{4}$ in Fig. 3.

B. Stability of surface states of MWSM

In this section, we show that, although the MWSM appears similar to a DSM, the Fermi arcs are topologically robust, and it is ultimately distinct from previous TSMs. The key difference is that DSM Fermi arcs may be separated from their Dirac nodes with certain symmetry-preserving perturbations [59]; in contrast, WSMs have Fermi arcs connected to their Weyl nodes irrespective of symmetry-preserving perturbation. To show MWSMs also share this robustness, we recall that MWSMs possess Euler topology due to their $\mathcal{T}' = \mathcal{T}\mathcal{I}$ symmetry. Therefore, with the aid of Qsymm [60], we check for combinations of $\tau^i \sigma^j$ ($i, j = x, y, z, 0$) which preserve just \mathcal{T}' . Consequently, the following satisfy our criterion: $\tau^x \sigma^x$, $\tau^y \sigma^y$, $\tau^z \sigma^z$, $\tau^x \sigma^y$, and $\tau^y \sigma^x$. Employing these perturbations in our system, we plot the corresponding Fermi arc contours. From the plots shown in Fig. S15 in the Supplemental Material [56], we can show that these \mathcal{T}' -only preserving perturbations do not disconnect the Fermi arcs from the nodes, and the Fermi

arc states are topologically protected, unlike the case for the DSM.

C. Fermi arcs for the MWSM as a stack of MCIs

WSMs can be interpreted as a set of CIs, each defined in a 2D submanifold of the 3D BZ of the WSM (e.g., each k_x - k_y plane) for a given value of k_z , stacked in the k_z direction. The Weyl nodes then correspond to topological phase transitions—corresponding to gap closings—in the stack between intervals in k_z with topologically distinct CIs. Specifically, we use the Qi-Wu-Zhang (QWZ) model [61], $\mathcal{H}_{\text{CI}} = B(2 + M - \cos k_x - \cos k_y)\sigma^z + \sin k_x\sigma^x + \sin k_y\sigma^y$ in particle-hole space. In the WSM, the mass term is given as $M = \gamma - \cos k_z$. Here, for the range $-1 < \gamma < 1$, $k_z \in [-\cos^{-1} \gamma, \cos^{-1} \gamma]$. The Fermi arcs we observe in the 2D BZ defined in the k_y - k_z for open boundary conditions in the x direction are projections of the chiral edge states of the slices of the corresponding CIs in the stack.

The multiplicative counterpart of a CI was introduced recently by Cook and Moore [54] as an MCI. Here, by construction, the MCI has two mass terms derived from each of the parent systems, one from each of the parent systems. Hence, there exists more than one way to stack the MCIs in the k_z direction. For instance, either the mass term of a single parent can be k_z dependent, or both can be. Here, we have defined the momentum dependence in both of the mass terms such that the difference in parent mass parameters remains constant. This is the case when $M_1 = \gamma_1 - \cos k_z$ and $M_2 = \gamma_2 - \cos k_z$, which leads to a certain linear path in the M_1 - M_2 phase diagram as a function of k_z , which is the trend we observe from our Wannier spectra plots in the parallel case in Fig. 4 derived from a stacking of MCI parallel systems and illustrated for two different cases in Fig. 7.

We then characterize the multiplicative Fermi arc states by opening boundary conditions in the x and y directions and plotting the the sum of the probability densities for the 40 eigenstates nearest in energy to zero. We show this in Fig. 8 for $k_z = 0$ (a 2D submanifold of the BZ realizing an MCI with both parents topologically nontrivial) and $k_z = \frac{\pi}{2}$ (a 2D submanifold of the BZ in which only one parent is topologically trivial). For the former case with parents shown in Figs. 8(a) and 8(b), the probability density in the corresponding child as shown in Fig. 8(c) is localized at sites at the boundary as well as at the sites adjacent to these sites. For the latter case, parent 1 has edge states, and parent 2 does not, as shown in Figs. 8(d) and 8(e). The resultant child probability density shows low-energy states localize only at the boundary sites, as shown in Fig. 8(f). We discussed in Sec. III F that a pair of Euler numbers should provide us a characterization of the bulk topology. Here, we observe the direct bulk boundary correspondence. The Euler number pair (2,0) links to the case where both k_z slices are topological, as shown in Fig. 8(c). When one slice is topological while the other is trivial, it corresponds to the Euler number pair (1, 1) and the localization in Fig. 8(f). This localization behavior is similar to that of the multiplicative Kitaev chain presented in a second work [62] by the present authors, where, if each parent is topological, edge states are localized at lattice sites right at the edge, but also at sites adjacent to these sites. We expect such

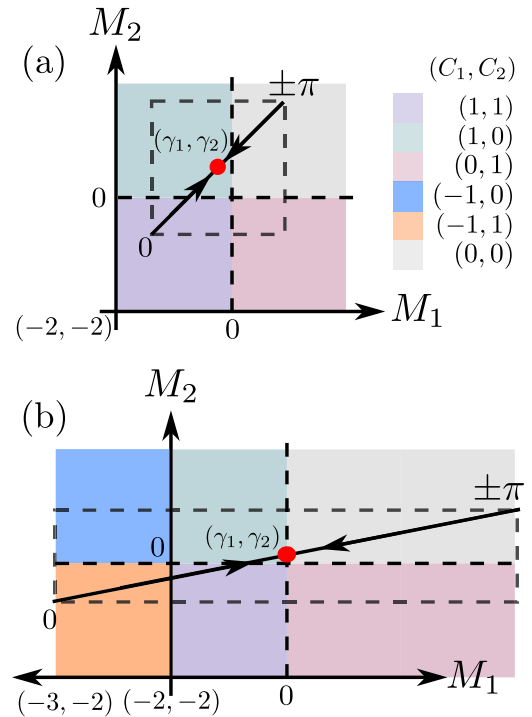


FIG. 7. The argument that multiplicative Weyl semimetal (MWSM) is a stacking of multiplicative Chern insulator (MCI) parallel systems only applies in the parallel case. The solid black line shows the stacking direction, with arrows indicating change with k_z . The red dot indicates the point at $k_z = \frac{\pi}{2}$. We show two cases: (a) where both the parents have only $C_{1,2} = 1$ Chern number regions and (b) where parent 1 has $C_1 = 1, -1$ Chern numbers, while parent 2 has only $C_2 = 1$ Chern number regions. The case (b) corresponds to Sec. IV D where we get edge states separate from the bulk.

localization to protect the edge states from backscattering to some extent, which we will explore in future work. Additionally, we note that the peaks in probability densities near the corners of the lattice reflect corner modes coexisting with edge modes in the low-energy manifold, with an example probability density for an individual corner mode shown in Figs. S16 and S17 in the Supplemental Material [56] for two separate cases. Similar corner modes appear for gapless symmetry-protected topological (SPT) phases realized by combining a topological insulator parent Hamiltonian and a critical, gapless parent Hamiltonian in the symmetry-protected multiplicative construction to form a child Hamiltonian [63]. In these cases, however, the corner modes derive from known models for gapless SPT phases realized within the child Hamiltonian. In future work, we will explore more general characterization of the rich bulk-boundary correspondence of multiplicative topological phases and to understand the coexistence of edge and corner modes as well as the broader link between multiplicative topological phases and SPT phases.

D. Boundary states disconnected from bulk states

The MCI can exhibit topologically robust yet floating edge states which are separated from the bulk by a finite energy gap

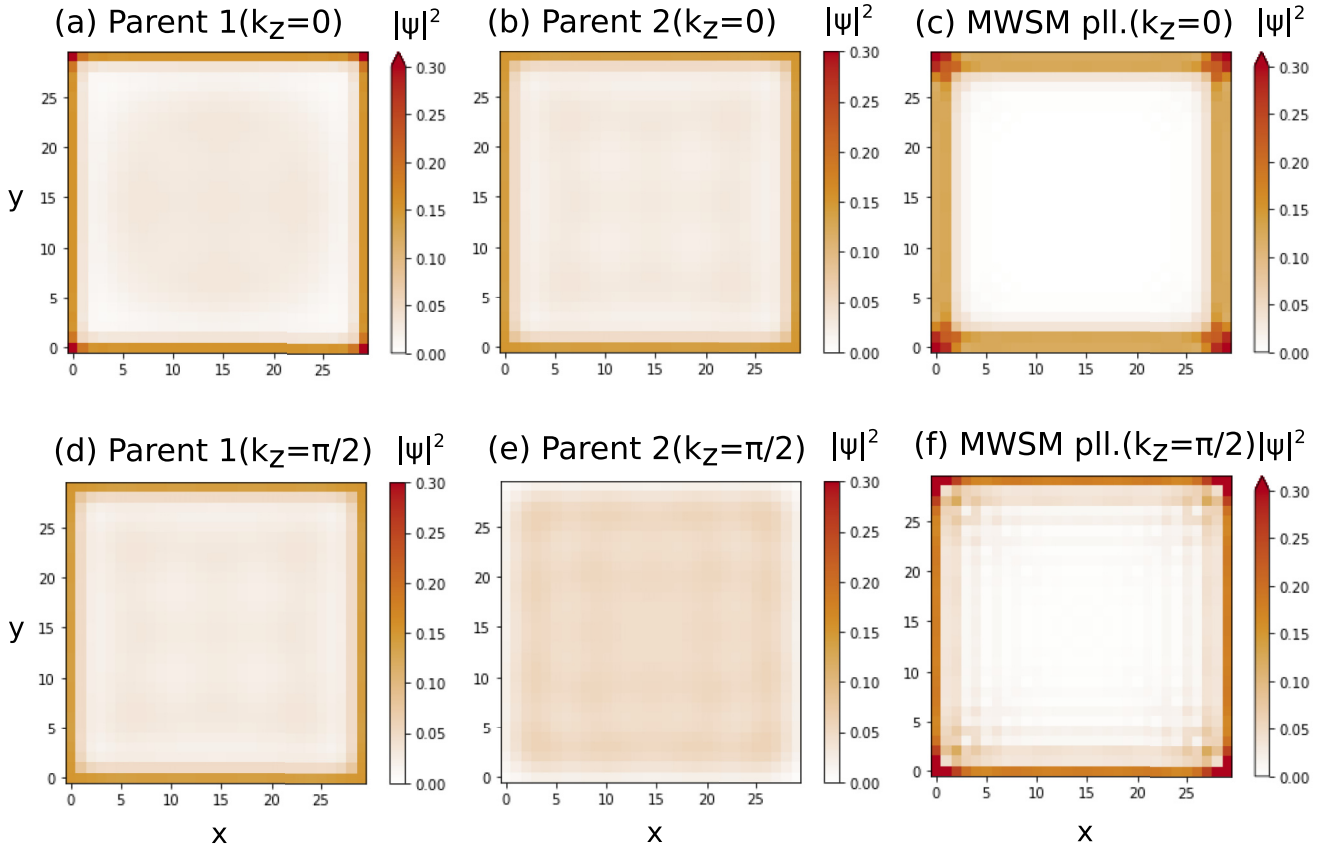


FIG. 8. Probability densities of superposition of 40 edge state eigenvectors in a $30 \times 30 (L_x \times L_y)$ square lattice at $k_z = 0$ and $k_z = \frac{\pi}{2}$ for (a) and (d) parent Weyl semimetal (WSM) 1 ($\gamma_1 = -0.5$), (b) and (e) parent WSM 2 ($\gamma_2 = 0.5$), and (c) and (f) multiplicative WSM (MWSM)|| child ($\gamma_1 = -0.5$ and $\gamma_2 = 0.5$), respectively. At $k_z = 0$, both the parent systems are topological, as seen from a visible edge state which results in localization at both the edge and second last edge sites in the MWSM|| child system. When $k_z = \frac{\pi}{2}$, parent 1 is still topological, but parent 2 is trivial, as seen from the absence of edge states which results in localization only at the edge sites of the MWSM|| child system.

[54]. MTSMs constructed from MCIs can inherit this exotic boundary state connectivity.

To realize this in a MWSM, we first need to consider the Hamiltonian for the MCI:

$$\mathcal{H}_{\text{CI},p1}(\mathbf{k}) = B_1(2 + M_1 - \cos k_x - \cos k_y)\tau^z + \sin k_x \tau^x + \sin k_y \tau^y, \quad (23a)$$

$$\mathcal{H}_{\text{CI},p2}(\mathbf{k}) = B_2(2 + M_2 - \cos k_x - \cos k_y)\sigma^z + \sin k_x \sigma^x + \sin k_y \sigma^y, \quad (23b)$$

$$\begin{aligned} \mathcal{H}_{\text{MCI},c}(\mathbf{k}) &= [B_1(2 + M_1 - \cos k_x - \cos k_y)\tau^z \\ &+ \sin k_x \tau^x + \sin k_y \tau^y] \\ &\otimes [-B_2(2 + M_2 - \cos k_x - \cos k_y)\sigma^z \\ &- \sin k_x \sigma^x + \sin k_y \sigma^y]. \end{aligned} \quad (23c)$$

To achieve the edge spectrum finitely gapped from the bulk, we require the parameter regime $M_1 \in [-4, -2]$ and $M_2 \in [-2, 0]$, which corresponds to Chern numbers $C = -1$ and $+1$, respectively.

Therefore, to construct a MWSM with such an edge spectrum, we choose one parent WSM where the Weyl nodes are separated in \mathbf{k} space by a stack of CIs, each with Chern number $C = +1$, and the Weyl nodes of the other parent are separated by a stack of CIs, each with Chern number

$C = -1$. Comparing Eq. (24a) with Eq. (23a) and Eq. (24b) with Eq. (23b), it is clear that, for each CI in the stack, the following mapping holds: $M_i = \gamma_i - \cos k_z$, $i \in \{1, 2\}$, where i labels the parent. From this mapping, it is not possible to have $M_2 \in (-4, -2)$ while $\gamma_i \in (-1, 1)$, $i \in \{1, 2\}$. We therefore generalize the mapping to the following form: $M_i = \gamma_i - r_i \cos k_z$, $i \in \{1, 2\}$, so that the parents and the child Hamiltonian for the MWSM parallel are

$$\begin{aligned} \mathcal{H}_{p1}(\mathbf{k}) &= t_{11} \sin k_x \tau^x + t_{21} \sin k_y \tau^y \\ &+ t_{31}(2 + \gamma_1 - \cos k_x - \cos k_y - r_1 \cos k_z)\tau^z, \end{aligned} \quad (24a)$$

$$\begin{aligned} \mathcal{H}_{p2}(\mathbf{k}) &= t_{12} \sin k_x \sigma^x + t_{22} \sin k_y \sigma^y \\ &+ t_{32}(2 + \gamma_2 - \cos k_x - \cos k_y - r_2 \cos k_z)\sigma^z, \end{aligned} \quad (24b)$$

$$\begin{aligned} \mathcal{H}_c(\mathbf{k}) &= [t_{11} \sin k_x \tau^x + t_{21} \sin k_y \tau^y \\ &+ t_{31}(2 + \gamma_1 - \cos k_x - \cos k_y - r_1 \cos k_z)\tau^z] \\ &\otimes [-t_{12} \sin k_x \sigma^x + t_{22} \sin k_y \sigma^y - t_{32}(2 + \gamma_2 \\ &- \cos k_x - \cos k_y - r_2 \cos k_z)\sigma^z]. \end{aligned} \quad (24c)$$

To construct one parent with the Chern number of this stack nontrivial and opposite in sign to the Chern number of the stack in the other parent, we first introduce some terminology.

We refer to the region between Weyl nodes including $k_z = 0$ as the regular Weyl region (RWR) and the region including $k_z = \pm\pi$ as the irregular Weyl region (IWR). The existence of Weyl nodes requires $|\gamma_{1,2}| \geq 1$ for $|\gamma_{1,2}| < 1$. It is then possible to realize a RWR with a negative Chern number by varying $r_{1,2}$, so that $\gamma_{1,2} - r_{1,2} \cos k_z \in (-4, -2)$. These RWRs—one of each parent system—must then occur over the same interval in k_z , however, to realize topological floating surface states. We set $\gamma_1 = 0$ and $r_1 = 3$, which means we have $C = -1$ for the range $[-\cos^{-1}(\frac{2}{3}), \cos^{-1}(\frac{2}{3})]$ when $M_1 = \gamma_1 - r_1 \cos k_z \in [-3, -2]$. Then we must have $\gamma_2 = \cos \frac{\pi}{3} = 0.5$ and $r_2 = 1$, so that in the region $k_z \in [-\cos^{-1}(\frac{2}{3}), \cos^{-1}(\frac{2}{3})]$, we have the same kind of MCI with edge states separated from the bulk as described in previous work [54]. These results are shown in Fig. 9. This case can also be represented as a stack of MCI parallel systems, but the regions vary with parent Chern number pairs ranging between (0,0), (0,1), (0,-1), (1,0), (1,1), and (1,-1), as shown in Fig. 7(b).

The MWSM \perp case of topologically robust yet floating Fermi arc surface states is constructed similarly, and we defer thorough investigation of this case to later work.

V. EFFECT OF MAGNETIC FIELD ON MWSM AND CHIRAL ANOMALY

We now investigate response signatures of MTSMs. As we consider MWSMs here, which may be constructed from WSM parent systems, we focus particularly on the question of whether there is a multiplicative generalization of the chiral anomaly, one of the most important signatures of WSMs: Application of nonorthogonal electric and magnetic fields can pump electrons between Weyl nodes of opposite chirality [64]. More specifically, applying an external magnetic field parallel to the axis along which Weyl nodes are separated in \mathbf{k} space yields a single chiral Landau level (LL) near each of the Weyl nodes. In WSMs, this suppresses backscattering of electrons with opposite chirality, manifesting as negative magnetoresistance (MR). WSMs therefore serve as condensed matter platforms for study of the chiral anomaly, also known as the Adler-Bell-Jackiw anomaly, associated with the standard model of particle physics [24,65,66]. When the external magnetic field is instead oriented perpendicular to the \mathbf{k} -space axis along which Weyl nodes are separated, semiclassical calculations indicate the presence of quantum oscillations in the density of states [19], observable in magnetization, magnetic torque, and MR measurements [66,67].

To study the effects of external fields on the MWSM, we first derive the LL structure for the WSM in the cases of external magnetic fields applied parallel and perpendicular to the Weyl node axis. We can then draw parallels between these results and their generalizations in the case of the MWSM.

A. Chiral anomaly in WSM

To study the chiral anomaly in a WSM, we consider a particular Bloch Hamiltonian $H_{\text{WSM}}(\mathbf{k})$ characterizing a WSM phase and its expansion around the k_z axis, i.e., $\mathbf{k} \rightarrow (0, 0, k_z)$

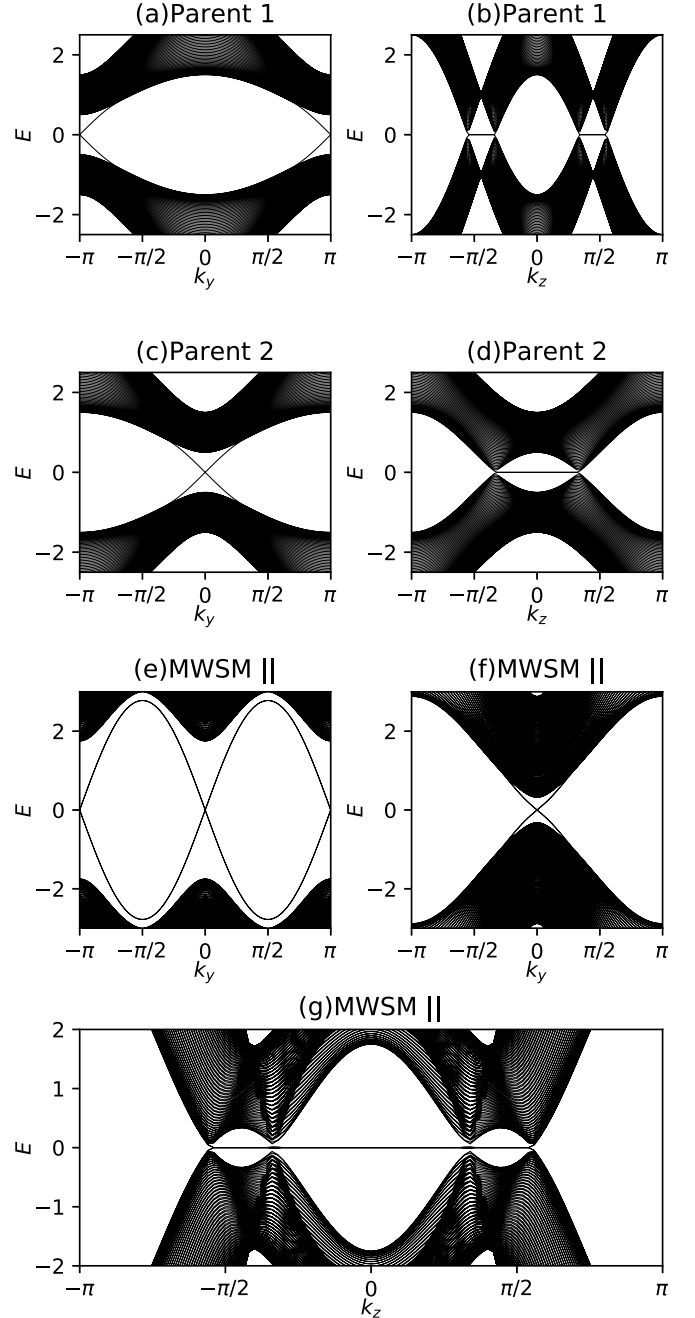


FIG. 9. Slab spectra along (a) k_y and (b) k_z for Weyl semimetal (WSM) parent 1 with $\gamma_1 = 0$, $r_1 = 3$, and slab spectra along (c) k_y ($k_z = 0$) and (d) k_z ($k_y = 0$) for WSM parent 2 with $\gamma_2 = \frac{2}{3}$, $r_2 = 1$, respectively. Corresponding slab spectra for the multiplicative WSM (MWSM)|| with $t_{11} = t_{12} = 1$, $t_{21} = t_{22} = 1$, and $t_{31} = t_{32} = 1$ along (e) k_y ($k_z = 0$), (f) k_y ($k_z = \frac{\pi}{2} - 0.1$), and (f) k_z ($k_y = 0$), respectively, with edges separate from the bulk slab spectra along k_y .

(up to second order in k_x and k_y):

$$\begin{aligned}
 H_{\text{WSM}}(\mathbf{k}) &= t(2 + \gamma - \cos k_x - \cos k_y - \cos k_z)\sigma^z \\
 &\quad + t' \sin k_y \sigma^y + t' \sin k_x \sigma^x, \\
 &\approx t \left[Q + \frac{1}{2}(k_x^2 + k_y^2) \right] \sigma^z + t' k_y \sigma^y + t' k_x \sigma^x,
 \end{aligned} \tag{25}$$

where $Q = \gamma - \cos k_z$. Applying the magnetic field $\mathbf{B} = B\hat{z}$ along the Weyl node axis, Peierls substitution changes the momenta in the following way: $k_x \rightarrow k'_x = k_x$, $k_y \rightarrow k'_y = k_y + eBx$, and $k_z \rightarrow k'_z = k_z$. The position-momentum commutator implies $[k'_y, k'_x] = ieB$, so that it is possible to define bosonic ladder operators:

$$a = \frac{k'_x - ik'_y}{\sqrt{2eB}}, \quad a^\dagger = \frac{k'_x + ik'_y}{\sqrt{2eB}}, \quad [a, a^\dagger] = 1. \quad (26)$$

Applying Eq. (26) after substituting $\mathbf{k} \rightarrow \mathbf{k}'$, we get the following system which looks like the polariton-conserving Jaynes-Cummings Hamiltonian:

$$H_{\text{WSM}}(\mathbf{k}') \approx t \left[Q + eB \left(a^\dagger a + \frac{1}{2} \right) \right] \sigma^z + t' \sqrt{2eB} (a \sigma^+ + a^\dagger \sigma^-), \quad (27)$$

where $\sigma^\pm = \frac{1}{2}(\sigma^x \pm i\sigma^y)$ are the spin-ladder operators in the basis $\{|+\rangle, |-\rangle\}$ of σ^z ($\sigma^z|\pm\rangle = \pm|\pm\rangle$). The ground state from the above Hamiltonian is given by the eigenvector $|\psi_{\text{LLL}}\rangle = |0; -\rangle$ (states denoted as $|n; s\rangle$, where n is the bosonic number and s is the spin direction), which leads to the lowest LL (LLL) energy:

$$E_{\text{LLL}} = -t \left(Q + \frac{1}{2} eB \right). \quad (28)$$

Near each of the Weyl nodes, it is easy to observe that $|\psi_{\text{LLL}}\rangle$ is chiral, as shown in Fig. 10. The other LLs can be derived by restricting to the 2D disjoint spaces $\{|n, -\rangle, |n-1, +\rangle\}$, parameterized by the bosonic number n , so that in each such basis, the Hamiltonian is

$$H(k_z, n) = -\frac{teB}{2} \sigma^0 - t(Q + eBn) \sigma^z + t' \sqrt{2eBn} \sigma^x. \quad (29)$$

The energy for the other LLs parameterized by $n = 1, 2, \dots$ is given by the eigenvalues of Eq. (29):

$$E_{n\text{LL}} = -\frac{teB}{2} \pm \sqrt{t^2(Q + eBn)^2 + 2t'^2 eBn}. \quad (30)$$

We have illustrated the analytically calculated LLs in Fig. 10 and compared them to numerical calculations of LLs. The numerical computation involves plotting the bands for the Peierls-substituted WSM with periodic boundary conditions, say, in the x direction, and subjected to a magnetic field in integer multiples of $\frac{2\pi}{L}$, where L is the size of the lattice in the x direction. We observe that the chiral LL from both analytical and numerical methods overlap, with an approximate overlap of the other LLs since we only considered until second order in k_x and k_y .

Next, we consider the case when the magnetic field is directed perpendicular to the Weyl node axis, say, $\mathbf{B} = B\hat{y}$. Expanding the first line of Eq. (25) around the Weyl node $\mathbf{k} = (0, 0, k_0 = \cos^{-1} \gamma)$ of positive chirality and setting $t = t' = 1$, we get

$$H_{\text{WSM}}(\mathbf{k}) \approx \sin k_0 (k_z - k_0) \sigma^z + k_y \sigma^y + k_x \sigma^x, \\ \Rightarrow H'_{\text{WSM}}(\mathbf{k}) \approx -k_y \sigma^z + k_x \sigma^x + \sin k_0 (k_z - k_0) \sigma^y, \quad (31)$$

where in the second line we have rotated the Hamiltonian to a new basis via $\sigma^x \rightarrow \sigma^z$ and $\sigma^y \rightarrow -\sigma^x$. In the presence

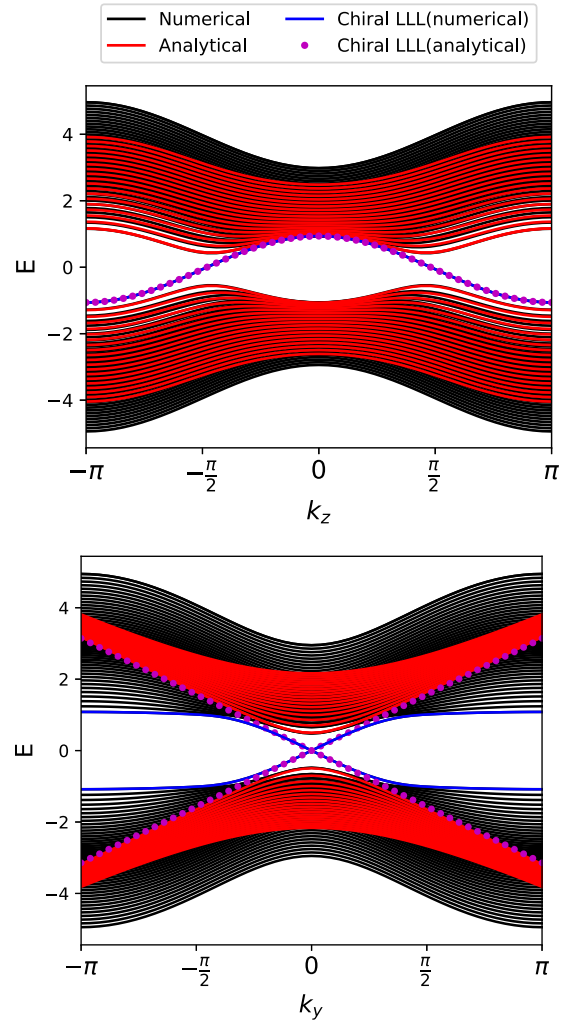


FIG. 10. Landau levels (LLs) for the two-band Weyl semimetal calculated analytically from Eq. (27) and numerically, with $t = 1 = t'$, $\gamma = 0$, and $\mathbf{B} = \frac{2\pi}{51} \hat{z}$ (upper) and $\mathbf{B} = \frac{2\pi}{51} \hat{y}$ (lower). The black bands indicate the numerically calculated LLs and the red bands the analytically calculated LLs for $n = 1, 2, \dots, 19$. The blue band and the dotted magenta band are the lowest LL (LLL) calculated numerically and analytically and are responsible for the chiral anomaly in the upper figure and Weyl orbits in the lower figure.

of the mentioned magnetic field perpendicular to the Weyl node axis, Peierls substitution is applied as $k_x \rightarrow k'_x = k_x$, $k_y \rightarrow k'_y = k_y$, and $k_z \rightarrow k'_z = k_z - eBx$. The commutation relation $[k_x, \sin k_0 (k_z - k_0 - eBx)] = ieB \sin k_0$ then constructs the bosonic ladder operators:

$$b = \frac{k_z - k_0 - eBx - ik_x}{\sqrt{2eB \sin k_0}}, \\ b^\dagger = \frac{k_z - k_0 - eBx + ik_x}{\sqrt{2eB \sin k_0}}. \quad (32)$$

The system in Eq. (31) then changes to

$$H_{\text{WSM}}(\mathbf{k}') \approx -k_y \sigma^z + \sqrt{2eB \sin k_0} (b \sigma^+ + b^\dagger \sigma^-). \quad (33)$$

Like the previous case, it is possible to resolve the Hamiltonian into the subspaces spanned by $\{|n, -\rangle, |n-1, +\rangle\}$,

where n is the eigenvalue of the number operator $b^\dagger b$. We get two chiral LLLs with energies $E = \pm k_y$ in the bulk, which are responsible for the chiral anomaly [66].

B. Chiral anomaly in the MWSM

We now study the response of the MWSM to external fields for comparison with the signatures of the chiral anomaly in the WSM reviewed in the previous section. We treat the MWSM parallel and perpendicular cases separately, given the expected sensitivity of the response to orientation of the axes of node separation relative to the orientation of the external fields.

1. LLs in the MWSM parallel system

In Sec. III A, we have derived the Dirac Hamiltonian for the MWSM|| in the vicinity of each of its two nodes $(0, 0, k_{01})$ and $(0, 0, k_{02})$ derived, respectively, from each of its two parents:

$$\begin{aligned} H_{||,1}^c(\mathbf{k}) &= (t'_1 k_x \tau^x + t'_1 k_y \tau^y + t_1 \sin k_{01} \bar{k}_{z,1} \tau^z) t_2 (\gamma_1 - \gamma_2) \sigma^z, \\ H_{||,2}^c(\mathbf{k}) &= t_1 (\gamma_1 - \gamma_2) \\ &\quad \times \tau^z (-t'_2 k_x \sigma^x + t'_2 k_y \sigma^y - t_2 \sin k_{02} \bar{k}_{z,2} \sigma^z), \end{aligned}$$

where $\bar{k}_{z,i} = k_z - k_{0,i}$ ($i = 1, 2$). In this section, we will only consider cases where $\gamma_1 \neq \gamma_2$. To investigate the response to external fields for the MWSM||, we consider the effect of the magnetic field along the Weyl node axis, i.e., $\mathbf{B} = B\hat{z}$. We use the exact Peierls substitution in Eq. (26), so that the two expressions above transform as follows:

$$\begin{aligned} H_{||,1}^c(\mathbf{k}') &= t_2 (\gamma_1 - \gamma_2) [t_1 \sin k_{01} \bar{k}_{z,1} \tau^z + t'_1 \sqrt{2eB} \\ &\quad \times (a\tau^+ + a^\dagger \tau^-)] \sigma^z, \\ H_{||,2}^c(\mathbf{k}') &= t_1 (\gamma_1 - \gamma_2) \tau^z [-t_2 \sin k_{02} \bar{k}_{z,2} \sigma^z - t'_2 \sqrt{2eB} \\ &\quad \times (a\sigma^- + a^\dagger \sigma^+)]. \end{aligned} \quad (34)$$

Here, $\tau^\pm = \frac{1}{2}(\tau^x \pm i\tau^y)$ and $\sigma^\pm = \frac{1}{2}(\sigma^x \pm i\sigma^y)$ are the pseudospin ladder operators in the τ and σ spaces. The LLLs from the above two expressions are given below:

$$\begin{aligned} H_{||,1}^c &\rightarrow E_{1,LLL} = \pm (\gamma_1 - \gamma_2) t_1 t_2 \sin k_{01} \bar{k}_{z,1}, \\ |\psi_{1,LLL}\rangle &= |0; -, \pm\rangle, \\ H_{||,2}^c &\rightarrow E_{2,LLL} = \mp (\gamma_1 - \gamma_2) t_2 t_2 \sin k_{02} \bar{k}_{z,2}, \\ |\psi_{2,LLL}\rangle &= |0; \pm, +\rangle. \end{aligned} \quad (35)$$

One may notice that the eigenvector $|0; -, +\rangle$ occurs in the vicinity of each node. Therefore, we calculate its energy eigenvalue if one expands the MWSM parallel system in the vicinity of the k_z axis. The details of the calculation can be found in Supplemental Material Sec. S3 [56]. We find the energy is given as

$$E_{|0; -, +\rangle} = [Q_1 Q_2 + \frac{1}{2} eB (Q_1 + Q_2)]. \quad (36)$$

We show that this expression is consistent with the numerically calculated LLs in Fig. 11. The other chiral LL is consistent with the other two eigenvectors $|0; -, -\rangle$ and $|0; +, +\rangle$ near their respective Weyl nodes. However, it appears distinct from $|0; -, +\rangle$ away from the Weyl nodes.

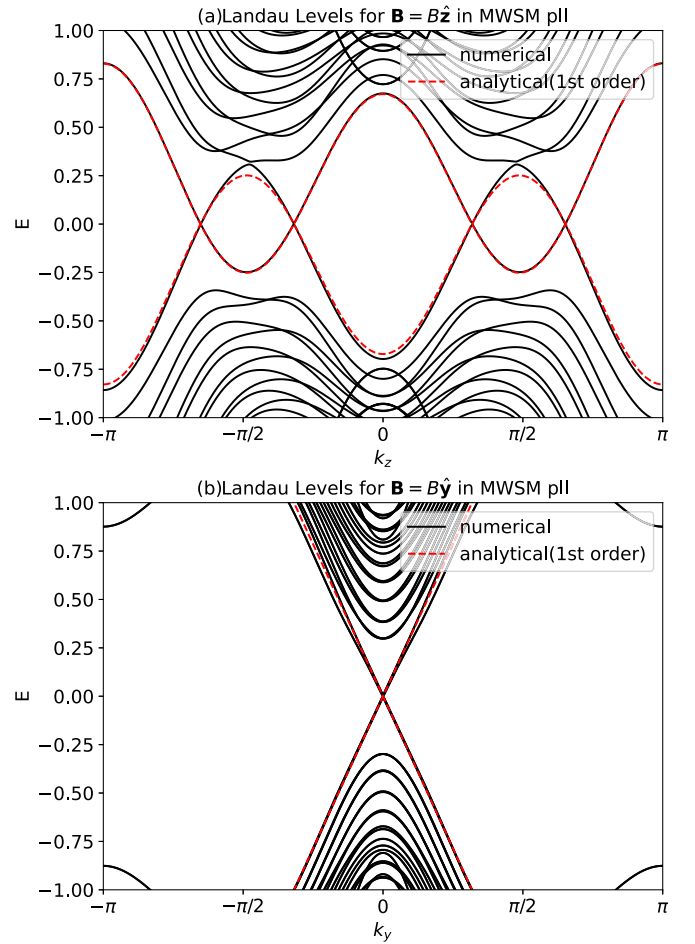


FIG. 11. The Landau levels (LLs) for the multiplicative Weyl semimetal (MWSM) parallel Hamiltonian with $\gamma_1 = -0.5$, $\gamma_2 = 0.5$, $t_1 = t'_1 = t_2 = t'_2 = 1$, and $B = \frac{2\pi}{80}$. (a) and (b) LLs for the magnetic field along the Weyl axis and perpendicular to the Weyl axis [at Weyl node $(0, 0, \frac{\pi}{3})$], respectively. The red bands refer to the lowest LLs, and the black bands form the bulk LLs.

In Fig. 11, for certain values of γ_1 and γ_2 , it appears at first glance as if there are two separate chiral LLs corresponding to $|0; -, -\rangle$ and $|1; -, -\rangle$, respectively. All four Weyl nodes are connected by each of these LLLs, however, and the two LLLs in combination furthermore account for each chirality at each node. Although this is reminiscent of the DSM, there is potentially a distinction in character between the chiralities at each node. If each parent corresponds to a particular degree of freedom (dof), for instance, and these dofs are physically distinct from one another in some sense, such as one parent corresponding to a twofold valley dof and the other corresponding to a twofold layer dof, the chiral anomalies are inequivalent and do not compensate one another as they would for a DSM.

The two apparently separated LLLs seem to only scatter between the Weyl nodes derived from their respective parents, i.e., intraparent scattering. Upon closer inspection, however, we see the intersection point between two apparently separated LLs is actually a very small gap. We have verified in Supplemental Material Sec. S3 [56] that the gap is finite in analytical calculations performed to second order

in momenta. The gap is an emergent feature of the multiplicative chiral anomaly, with the single LLL reducing to $|0; -, -\rangle$ and $|0; +, +\rangle$ at nodes associated with a particular parent. We therefore interpret the multiplicative chiral anomaly as exhibiting parent-graded features as well as emergent features not associated with either individual parent. This is reminiscent of the topologically robust floating bands of the MCI [54].

A calculation like that yielding Eq. (33) provides the chiral LLLs for the MWSM parallel system when the magnetic field is oriented perpendicular to the Weyl axis along the y direction $\mathbf{B} = B\hat{y}$. We show this using the Hamiltonian up to linear order near the node derived from parent 1 calculated in Eq. (15). The LLL should have energies $E = \pm(\gamma_1 - \gamma_2)k_y$. However, this calculation also shows that the linear order calculations dominate only if the distance between parents 1 and 2 Weyl nodes are large. Otherwise, quadratic order effects become more significant. This is expected since quadratic order effects affect the chiral LLs when the magnetic field is parallel to the Weyl axis, as mentioned earlier. We defer further study of the details of such quadratic order effects to future work.

2. LLs in the MWSM perpendicular system

In Sec. III B, we have shown the linear expansion of the MWSM \perp Bloch Hamiltonian near each of the nodes corresponding to one parent with Weyl nodes separated along the k_y axis and that of the other parent along the k_z axis in Eqs. (18) and (19). Without loss of generality, we consider $t_{31} = t_{32} = t_{21} = t_{22} = 1 = t_{11} = t_{12}$. There exist three separate cases one needs to check: (i) the magnetic field along the Weyl axis of the first parent $\mathbf{B} = B\hat{y}$, (ii) the magnetic field along the Weyl axis of the second parent $\mathbf{B} = B\hat{z}$, and (iii) the magnetic field perpendicular to the Weyl axis of both parents $\mathbf{B} = B\hat{x}$. In cases where the magnetic field is parallel to one parent Weyl axis, we expand up to quadratic order in k_x and k_y to include the zero-point energy contribution.

(1) Case 1 ($\mathbf{B} = B\hat{y}$): Substituting $k_x \rightarrow k'_x = k_x + eBz$ and using the bosonic ladder operators $a_{\perp,y} = \frac{k_z - ik'_x}{\sqrt{2eB}}$, $a_{\perp,y}^\dagger = \frac{k_z + ik'_x}{\sqrt{2eB}}$, we have, from Eq. (18),

$$H_{\perp,1}(\mathbf{k}') = \left[(\sin k_{0,1}(k_y - k_{0,1}) + eB \left(a_{\perp,y}^\dagger a_{\perp,y} + \frac{1}{2} \right) \right] \tau^z + \sqrt{2eB} (a_{\perp,y} \tau^+ + a_{\perp,y}^\dagger \tau^-) \otimes [\sin k_{0,1} \sigma^y + (\gamma_1 - \gamma_2) \sigma^z]. \quad (37)$$

For the expression from Eq. (19), we instead consider the following bosonic ladder operators: $\tilde{a}_{\perp,y} = \frac{k_z - ik'_x}{\sqrt{2eB \sin k_{0,2}}}$ and $\tilde{a}_{\perp,y}^\dagger = \frac{k_z + ik'_x}{\sqrt{2eB \sin k_{0,2}}}$, which give us

$$H_{\perp,2}(\mathbf{k}') = [\sin k_{0,2} \tau^y + (\gamma_1 - \gamma_2) \tau^z] \otimes [k_y \sigma^y - \sqrt{2eB \sin k_{0,2}} (\tilde{a}_{\perp,y} \sigma_y^+ + \tilde{a}_{\perp,y}^\dagger \sigma_y^-)]. \quad (38)$$

It is easy to find the LLL energies in the vicinity of each node. From Eqs. (37) and (38), we respectively have the LLL

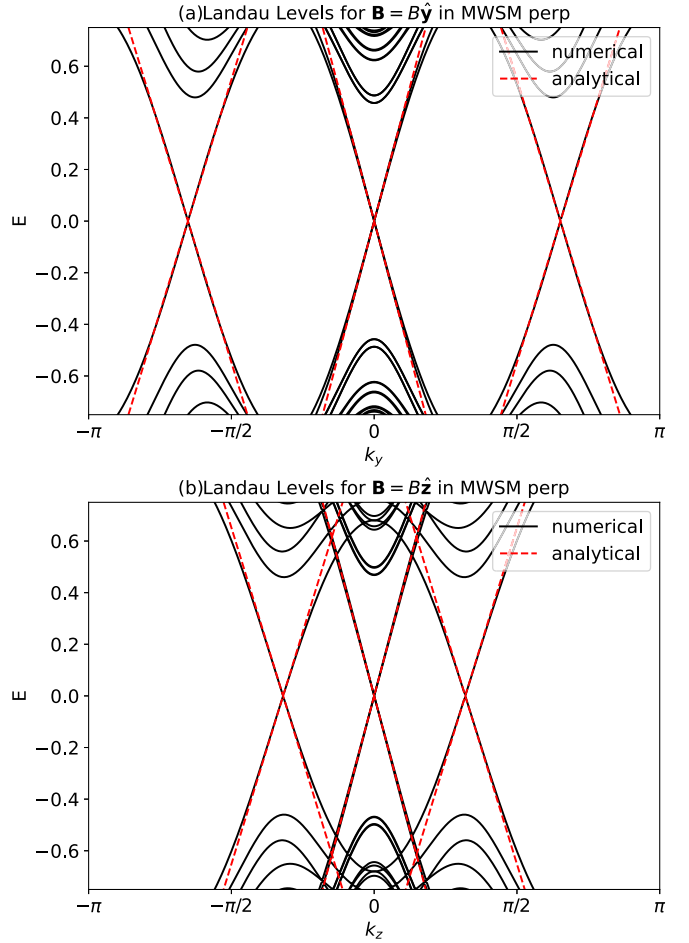


FIG. 12. Landau levels (LLs) for the multiplicative Weyl semimetal (MWSM) perpendicular system with $\gamma_1 = -0.5$ and $\gamma_2 = 0.5$ representing separation of Weyl nodes along the k_y and k_z directions, respectively. We show two cases: when the magnetic field is along the (a) y and (b) z directions. We have shown that lowest LLs calculated numerically match the analytical expressions (red dotted) from Eqs. (39) and (40) in (a) and (b), respectively, near the Weyl nodes. Since the magnetic field is parallel to one Weyl node separation and perpendicular to another, the above behavior is expected.

energies:

$$E_{y,1,LLL} = \pm \sqrt{\sin^2 k_{0,1} + (\gamma_1 - \gamma_2)^2} \times \left[\sin k_{0,1}(k_y - k_{0,1}) + \frac{1}{2}eB \right],$$

$$E_{y,2,LLL} = \pm \sqrt{\sin^2 k_{0,2} + (\gamma_1 - \gamma_2)^2} k_y. \quad (39)$$

We then find two k_y -dependent chiral LLLs connecting the nodes of the first parent, while we have two chiral LLLs at $k_y = 0$ due to the second parent, as shown in Fig. 12(a). The following result was expected if one considers the LLs for the parents for different directions of the magnetic field discussed in the previous subsection. For the MWSM perpendicular case, the incident magnetic field in this case is both parallel to the Weyl axis of parent 1 and perpendicular to the Weyl axis of parent 2, so that we get both kinds of LLs simultaneously.

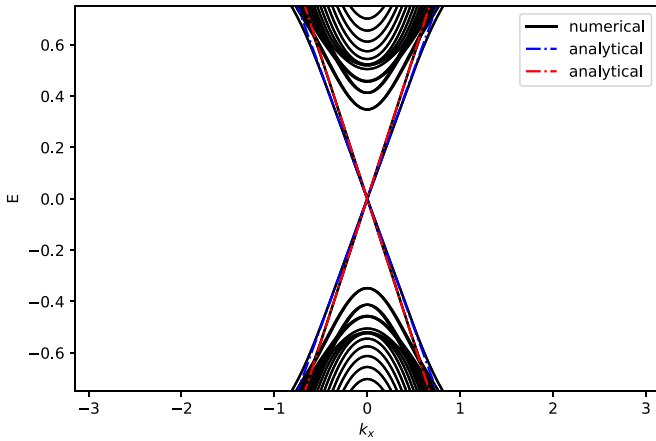


FIG. 13. Landau levels (LLs) for multiplicative Weyl semimetal (MWSM) perpendicular system with $\gamma_1 = 0.5$ and $\gamma_2 = 0.0$ with magnetic field $\mathbf{B} = B\hat{\mathbf{x}}$ (one flux quantum) perpendicular to Weyl axes of both parents. We plot at $\mathbf{k} = (0, 0, \frac{\pi}{2})$ which is the Weyl node of the second parent and find our analytical calculation in Eq. (41) fits the numerics near $k_x = 0$ for the lowest LLs.

(2) Case 2 ($\mathbf{B} = B\hat{\mathbf{z}}$): This produces results like Case 1, as shown in Fig. 12(b). A similar calculation gives us the LLL energies:

$$\begin{aligned} E_{z,1,LLL} &= \pm \sqrt{\sin^2 k_{0,1} + (\gamma_1 - \gamma_2)^2 k_z}, \\ E_{z,2,LLL} &= \pm \sqrt{\sin^2 k_{0,2} + (\gamma_1 - \gamma_2)^2} \\ &\quad \times \left[\sin k_{0,2}(k_z - k_{0,2}) + \frac{1}{2}eB \right]. \end{aligned} \quad (40)$$

(3) Case 3 ($\mathbf{B} = B\hat{\mathbf{x}}$): Since the magnetic field is perpendicular to both Weyl axes, we expect two types, in total four, of chiral LLs at $k_x = 0$. Each chiral LL corresponds to one of the nodes of the MWSM perpendicular system, and their energies can be calculated as follows:

$$\begin{aligned} E_{x,1,LLL} &= \pm \sqrt{\sin^2 k_{0,1} + (\gamma_1 - \gamma_2)^2 k_x}, \\ E_{x,2,LLL} &= \pm \sqrt{\sin^2 k_{0,2} + (\gamma_1 - \gamma_2)^2 k_x}. \end{aligned} \quad (41)$$

We illustrate this case in Fig. 13 for $\gamma_1 = 0.5$ and $\gamma_2 = 0.0$. Like the analytical calculation, we have two pairs of LLLs with different slopes, which hence must correspond to different velocities in the bulk contribution to the Weyl orbits. We look for such an effect on transport in a future work.

VI. DISCUSSION AND CONCLUSIONS

In this paper, we have introduced the previously unidentified MTSM phases of matter, distinguished by Bloch Hamiltonians with a symmetry-protected tensor product structure. Parent Bloch Hamiltonians, with either one or both of the parents being topologically nontrivial, may then be combined in the tensor product to realize MTSM phases inheriting topology from the parent states.

We consider foundational examples of MTSMs, with Bloch Hamiltonians constructed as tensor products of two-band Bloch Hamiltonians, each characterizing a WSM phase. These MTSM phases are protected by a combination of

symmetries of class DIII at the level of the child, and each parent Bloch Hamiltonian in class D. Given the great variety of exotic crystalline point group symmetries considered to protect most recently identified TSM phases, it is remarkable that the symmetry protection of these multiplicative semimetal phases is relatively simple and suggests many additional multiplicative semimetal phases may be identified by enforcing these many other symmetries on parent Bloch Hamiltonians. While this more extensive symmetry protection is largely beyond the scope of this paper, we do note that generalized time-reversal symmetry corresponding to invariance of the child Hamiltonian under operation $\mathcal{T}' = \mathcal{T}\mathcal{I}$, where \mathcal{T} is time reversal and \mathcal{I} is spatial inversion, also yields a multiplicative structure for parent Hamiltonians without particle-hole symmetry.

We first characterize MTSM phases in the bulk, showing the bulk spectrum of the child Bloch Hamiltonian depends in a multiplicative way on the spectra of the parent Bloch Hamiltonians: Each eigenvalue of the child, at a given point in \mathbf{k} space, is a product of eigenvalues, one from each parent. We furthermore consider two different constructions of the MWSM, either for the case of each parent having a pair of Weyl nodes separated along the same axis in \mathbf{k} space (parallel construction) or along perpendicular axes in \mathbf{k} space (perpendicular construction). For either construction, the multiplicative symmetry-protected structure can then naturally yield nodal degeneracies reminiscent of Dirac nodes or higher-charge Weyl nodes. However, the multiplicative degeneracies are distinguished from these more familiar quasiparticles by distinctive Wannier spectra signatures in the bulk and exotic bulk-boundary correspondence. Importantly, bulk characterization by Wannier spectra reveals a complex dependence of Berry connection in the child Bloch Hamiltonian on Berry connection of each parent Bloch Hamiltonian, depending on whether the parents are constructed with Weyl nodes separated along the same axis in momentum space (parallel) or not (perpendicular). Additionally, the connectivity of Fermi arc surface states for the MWSM is far more complex than in standard DSMs or WSMs, reflecting the underlying dependence of the child topology on the topology of the parents. An especially interesting example is the realization of topologically protected—yet floating—boundary states.

Response signatures of the MWSM also inherit response signatures of the parents, with the potential for emergent phenomena beyond that of either parent individually. Here, we consider the multiplicative analog of one of the defining response signatures of the WSM, the chiral anomaly, finding instead multiple coexisting chiral anomalies graded by the parent dofs as well as emergent features in the LL structure not inherited from a particular parent. In the case of parents corresponding to effectively the same dof, the response reduces to a signature reminiscent of a DSM. This brings up the possibility of controlled manipulation of particular properties of an electronic system like spintronics.

We briefly comment on features expected in more general cases of multiplicative topological phases to be explored in future work, either with parent Hamiltonians possessing larger matrix representations than 2×2 or with >2 parent Hamiltonians. For one, the dimensionality of the grandchild could be even higher relative to dimensionality of the parents than the dimensionality of a child with two parents. For another, one

could, in principle, imagine combining four different parent topological phases together, such as a Hopf insulator, WSM, CI, and topological one-dimensional superconductor. For just two parents, we can only combine two of these together, so physics of these more general multiplicative child Hamiltonians can be far richer than that discussed in this paper.

We also briefly speculate about the physical meaning of results for general twist angle θ between the parent Hamiltonians (and effectively parent lattices) considered in Sec. III C: While we only consider multiplicative child Hamiltonians to be quadratic in creation and annihilation operators in this paper, the multiplicative Hamiltonian may also be assigned a basis that is purely quartic in creation and annihilation operators. That is, the multiplicative Hamiltonian may be interpreted instead as a strong interaction term governing correlations between the parent systems. This alternative interpretation may be important in fully understanding the connection between the general θ multiplicative Hamiltonians and Moiré systems.

In future work, we will characterize other signatures of MTSMs anticipated given the extensive characterization of WSMs and DSMs, particularly optical and nonlinear

responses [68–74], given the tremendous interest in the bulk photovoltaic effect in WSMs, as well as symmetry protection of more exotic topological quasiparticles, such as multiplicative generalizations of multifold fermions or nodal lines. In a separate work studying the circular photogalvanic effect (CPGE) in MWSMs [75], in fact, we find quantization of the CPGE in the presence of perturbations spoiling quantization for WSMs and multifold fermions [68–72], indicating the promise of multiplicative topology in the search for truly topological response signatures akin to those of the quantum Hall effect. Given the immense body of work on TSMs and the surprising consequences of multiplicative topology for bulk-boundary correspondence, nodal band structure, and Berry phase structure, our introduction of previously unidentified MTSMs into the literature lays the foundation for considerable future theoretical and experimental study, which will greatly expand and deepen our understanding of TSM phases.

ACKNOWLEDGMENTS

We gratefully acknowledge helpful discussions with J. E. Moore, I. A. Day, R. Calderon, D. Varjas, and M. Pacholski.

-
- [1] A. A. Soluyanov, D. Gresch, Z. Wang, Q. Wu, M. Troyer, X. Dai, and B. A. Bernevig, *Nature (London)* **527**, 495 (2015).
- [2] B. Bradlyn, J. Cano, Z. Wang, M. G. Vergniory, C. Felser, R. J. Cava, and B. A. Bernevig, *Science* **353**, aaf5037 (2016).
- [3] S.-M. Huang, S.-Y. Xu, I. Belopolski, C.-C. Lee, G. Chang, B. Wang, N. Alidoust, G. Bian, M. Neupane, C. Zhang *et al.*, *Nat. Commun.* **6**, 7373 (2015).
- [4] B. Q. Lv, H. M. Weng, B. B. Fu, X. P. Wang, H. Miao, J. Ma, P. Richard, X. C. Huang, L. X. Zhao, G. F. Chen *et al.*, *Phys. Rev. X* **5**, 031013 (2015).
- [5] B. Q. Lv, N. Xu, H. M. Weng, J. Z. Ma, P. Richard, X. C. Huang, L. X. Zhao, G. F. Chen, C. E. Matt, F. Bisti *et al.*, *Nat. Phys.* **11**, 724 (2015).
- [6] S.-Y. Xu, N. Alidoust, I. Belopolski, Z. Yuan, G. Bian, T.-R. Chang, H. Zheng, V. N. Strocov, D. S. Sanchez, G. Chang *et al.*, and *Nat. Phys.* **11**, 748 (2015).
- [7] S.-Y. Xu, I. Belopolski, N. Alidoust, M. Neupane, G. Bian, C. Zhang, R. Sankar, G. Chang, Z. Yuan, C.-C. Lee *et al.*, *Science* **349**, 613 (2015).
- [8] S. Borisenko, Q. Gibson, D. Evtushinsky, V. Zabolotnyy, B. Büchner, and R. J. Cava, *Phys. Rev. Lett.* **113**, 027603 (2014).
- [9] Z. K. Liu, J. Jiang, B. Zhou, Z. J. Wang, Y. Zhang, H. M. Weng, D. Prabhakaran, S.-K. Mo, H. Peng, P. Dudin *et al.*, *Nat. Mater.* **13**, 677 (2014).
- [10] Z. K. Liu, B. Zhou, Y. Zhang, Z. J. Wang, H. M. Weng, D. Prabhakaran, S.-K. Mo, Z. X. Shen, Z. Fang, X. Dai *et al.*, *Science* **343**, 864 (2014).
- [11] M. Neupane, S.-Y. Xu, R. Sankar, N. Alidoust, G. Bian, C. Liu, I. Belopolski, T.-R. Chang, H.-T. Jeng, H. Lin *et al.*, *Nat. Commun.* **5**, 3786 (2014).
- [12] D. Wu, Z. Mi, Y. Li, W. Wu, P. Li, Y. Song, G. Liu, G. Li, and J. Luo, *Chin. Phys. Lett.* **36**, 077102 (2019).
- [13] X. Wan, A. M. Turner, A. Vishwanath, and S. Y. Savrasov, *Phys. Rev. B* **83**, 205101 (2011).
- [14] A. A. Burkov and L. Balents, *Phys. Rev. Lett.* **107**, 127205 (2011).
- [15] G. B. Halász and L. Balents, *Phys. Rev. B* **85**, 035103 (2012).
- [16] N. P. Armitage, E. J. Mele, and A. Vishwanath, *Rev. Mod. Phys.* **90**, 015001 (2018).
- [17] Y. Sun, S.-C. Wu, M. N. Ali, C. Felser, and B. Yan, *Phys. Rev. B* **92**, 161107(R) (2015).
- [18] Y. Baum, E. Berg, S. A. Parameswaran, and A. Stern, *Phys. Rev. X* **5**, 041046 (2015).
- [19] A. C. Potter, I. Kimchi, and A. Vishwanath, *Nat. Commun.* **5**, 5161 (2014).
- [20] A. Gyenis, H. Inoue, S. Jeon, B. B. Zhou, B. E. Feldman, Z. Wang, J. Li, S. Jiang, Q. D. Gibson, S. K. Kushwaha *et al.*, *New J. Phys.* **18**, 105003 (2016).
- [21] R. Batabyal, N. Morali, N. Avraham, Y. Sun, M. Schmidt, C. Felser, A. Stern, B. Yan, and H. Beidenkopf, *Sci. Adv.* **2**, e1600709 (2016).
- [22] Z. Rao, H. Li, T. Zhang, S. Tian, C. Li, B. Fu, C. Tang, L. Wang, Z. Li, W. Fan *et al.*, *Nature (London)* **567**, 496 (2019).
- [23] D. Rees, B. Lu, Y. Sun, K. Manna, R. Özgür, S. Subedi, H. Borrmann, C. Felser, J. Orenstein, and D. H. Torchinsky, *Phys. Rev. Lett.* **127**, 157405 (2021).
- [24] H. Nielsen and M. Ninomiya, *Phys. Lett. B* **130**, 389 (1983).
- [25] D. T. Son and B. Z. Spivak, *Phys. Rev. B* **88**, 104412 (2013).
- [26] S. A. Parameswaran, T. Grover, D. A. Abanin, D. A. Pesin, and A. Vishwanath, *Phys. Rev. X* **4**, 031035 (2014).
- [27] X. Huang, L. Zhao, Y. Long, P. Wang, D. Chen, Z. Yang, H. Liang, M. Xue, H. Weng, Z. Fang *et al.*, *Phys. Rev. X* **5**, 031023 (2015).

- [28] C.-L. Zhang, S.-Y. Xu, I. Belopolski, Z. Yuan, Z. Lin, B. Tong, G. Bian, N. Alidoust, C.-C. Lee, S.-M. Huang *et al.*, *Nat. Commun.* **7**, 10735 (2016).
- [29] C. Shekhar, A. K. Nayak, Y. Sun, M. Schmidt, M. Nicklas, I. Leermakers, U. Zeitler, Y. Skourski, J. Wosnitzer, Z. Liu *et al.*, *Nat. Phys.* **11**, 645 (2015).
- [30] F. Arnold, C. Shekhar, S.-C. Wu, Y. Sun, R. D. dos Reis, N. Kumar, M. Naumann, M. O. Ajeesh, M. Schmidt, A. G. Grushin *et al.*, *Nat. Commun.* **7**, 11615 (2016).
- [31] T. Graf, C. Felser, and S. S. Parkin, *Prog. Solid State Chem.* **39**, 1 (2011).
- [32] N. P. Butch, P. Syers, K. Kirshenbaum, A. P. Hope, and J. Paglione, *Phys. Rev. B* **84**, 220504(R) (2011).
- [33] F. F. Tafti, T. Fujii, A. Juneau-Fecteau, S. René de Cotret, N. Doiron-Leyraud, A. Asamitsu, and L. Taillefer, *Phys. Rev. B* **87**, 184504 (2013).
- [34] Y. Pan, A. M. Nikitin, T. V. Bay, Y. K. Huang, C. Paulsen, B. H. Yan, and A. de Visser, *Europhys. Lett.* **104**, 27001 (2013).
- [35] Y. Nakajima, R. Hu, K. Kirshenbaum, A. Hughes, P. Syers, X. Wang, K. Wang, R. Wang, S. R. Saha, D. Pratt *et al.*, *Sci. Adv.* **1**, e1500242 (2015).
- [36] Z. Fisk, P. C. Canfield, W. P. Beyermann, J. D. Thompson, M. F. Hundley, H. R. Ott, E. Felder, M. B. Maple, M. A. Lopez de la Torre, P. Visani *et al.*, *Phys. Rev. Lett.* **67**, 3310 (1991).
- [37] J. K. Kawasaki, A. Sharan, L. I. M. Johansson, M. Hjort, R. Timm, B. Thiagarajan, B. D. Schultz, A. Mikkelsen, A. Janotti, and C. J. Palmström, *Sci. Adv.* **4**, eaar5832 (2018).
- [38] S. Murakami, *New J. Phys.* **9**, 356 (2007).
- [39] Z. Wang, Y. Sun, X.-Q. Chen, C. Franchini, G. Xu, H. Weng, X. Dai, and Z. Fang, *Phys. Rev. B* **85**, 195320 (2012).
- [40] S. M. Young, S. Zaheer, J. C. Y. Teo, C. L. Kane, E. J. Mele, and A. M. Rappe, *Phys. Rev. Lett.* **108**, 140405 (2012).
- [41] N. B. Schröter, D. Pei, M. G. Vergniory, Y. Sun, K. Manna, F. De Juan, J. A. Krieger, V. Süß, M. Schmidt, P. Dudin *et al.*, *Nat. Phys.* **15**, 759 (2019).
- [42] C. L. Kane and T. C. Lubensky, *Nat. Phys.* **10**, 39 (2014).
- [43] J. Arkininstall, M. H. Teimourpour, L. Feng, R. El-Ganainy, and H. Schomerus, *Phys. Rev. B* **95**, 165109 (2017).
- [44] M. Kremer, I. Petrides, E. Meyer, M. Heinrich, O. Zilberberg, and A. Szameit, *Nat. Commun.* **11**, 907 (2020).
- [45] S. Yoshida, K. Yada, and Y. Tanaka, *Phys. Rev. B* **104**, 094506 (2021).
- [46] L. Song, H. Yang, Y. Cao, and P. Yan, *Nat. Commun.* **13**, 5601 (2022).
- [47] A. M. Marques and R. G. Dias, *Phys. Rev. B* **104**, 165410 (2021).
- [48] T. Mizoguchi, T. Yoshida, and Y. Hatsugai, *Phys. Rev. B* **103**, 045136 (2021).
- [49] H. Weyl, *Proc. Natl. Acad. Sci. USA* **15**, 323 (1929).
- [50] A. A. Zyuzin, S. Wu, and A. A. Burkov, *Phys. Rev. B* **85**, 165110 (2012).
- [51] T. Morimoto and A. Furusaki, *Phys. Rev. B* **89**, 235127 (2014).
- [52] J. E. Moore, Y. Ran, and X.-G. Wen, *Phys. Rev. Lett.* **101**, 186805 (2008).
- [53] A. Y. Kitaev, *Phys. Usp.* **44**, 131 (2001).
- [54] A. M. Cook and J. E. Moore, *Commun. Phys.* **5**, 262 (2022).
- [55] A. Dunbrack and J. Cano, *Phys. Rev. B* **107**, 235425 (2023).
- [56] See Supplemental Material at <http://link.aps.org/supplemental/10.1103/PhysRevB.109.035147> for details on Wilson loop, surface state spectra, Euler space topology, and Landau level calculations.
- [57] A. Alexandradinata, X. Dai, and B. A. Bernevig, *Phys. Rev. B* **89**, 155114 (2014).
- [58] Y. Guan, A. Bouhon, and O. V. Yazyev, *Phys. Rev. Res.* **4**, 023188 (2022).
- [59] M. Kargarian, M. Randeria, and Y.-M. Lu, *Proc. Natl. Acad. Sci. USA* **113**, 8648 (2016).
- [60] D. Varjas, T. Ö. Rosdahl, and A. R. Akhmerov, *New J. Phys.* **20**, 093026 (2018).
- [61] X.-L. Qi, Y.-S. Wu, and S.-C. Zhang, *Phys. Rev. B* **74**, 085308 (2006).
- [62] A. Pal, J. H. Winter, A. M. Cook, *Phys. Rev. B* **109**, 014516 (2024).
- [63] R. Flores-Calderón, E. König, and A. M. Cook, [arXiv:2311.17799](https://arxiv.org/abs/2311.17799).
- [64] S. Jia, S.-Y. Xu, and M. Z. Hasan, *Nat. Mater.* **15**, 1140 (2016).
- [65] J. S. Bell and R. W. Jackiw, *Nuov. Cim. A* **60**, 47 (1969).
- [66] B. Yan and C. Felser, *Annu. Rev. Condens. Matter Phys.* **8**, 337 (2017).
- [67] P. J. Moll, A. C. Potter, N. L. Nair, B. Ramshaw, K. A. Modic, S. Riggs, B. Zeng, N. J. Ghimire, E. D. Bauer, R. Kealhofer *et al.*, *Nat. Commun.* **7**, 12492 (2016).
- [68] F. Flicker, F. de Juan, B. Bradlyn, T. Morimoto, M. G. Vergniory, and A. G. Grushin, *Phys. Rev. B* **98**, 155145 (2018).
- [69] Z. Ni, B. Xu, M.-Á. Sánchez-Martínez, Y. Zhang, K. Manna, C. Bernhard, J. Venderbos, F. De Juan, C. Felser, A. G. Grushin *et al.*, *npj Quantum Mater.* **5**, 96 (2020).
- [70] M.-A. Sánchez-Martínez, F. de Juan, and A. G. Grushin, *Phys. Rev. B* **99**, 155145 (2019).
- [71] S. Kaushik and J. Cano, *Phys. Rev. B* **104**, 155149 (2021).
- [72] B. Xu, Z. Fang, M.-Á. Sánchez-Martínez, J. W. Venderbos, Z. Ni, T. Qiu, K. Manna, K. Wang, J. Paglione, C. Bernhard *et al.*, *Proc. Natl. Acad. Sci. USA* **117**, 27104 (2020).
- [73] F. de Juan, Y. Zhang, T. Morimoto, Y. Sun, J. E. Moore, and A. G. Grushin, *Phys. Rev. Res.* **2**, 012017(R) (2020).
- [74] A. Avdoshkin, V. Kozii, and J. E. Moore, *Phys. Rev. Lett.* **124**, 196603 (2020).
- [75] A. Pal, D. Varjas, and A. M. Cook, [arXiv:2312.03159](https://arxiv.org/abs/2312.03159).